

Multi-elemental Statistical Features of Early Paleogene Sediments from the Mid-latitude Eastern Indian Ocean

Yusuke Kuwahara^{1,2}, Kazutaka Yasukawa^{3,1}, Erika Tanaka^{4,3}, Kentaro Nakamura^{3,1,2}, Minoru Ikehara⁴, and Yasuhiro Kato^{1,2}

¹Department of Systems Innovation, School of Engineering, The University of Tokyo, 7-3-1 Hongo, Bunkyo-ku, Tokyo, 113-8656, Japan.

²Ocean Resources Research Center for Next Generation, Chiba Institute of Technology, 2-17-1 Tsudanuma, Narashino, Chiba, 275-0016, Japan.

³Frontier Research Center for Energy and Resources, School of Engineering, The University of Tokyo, 7-3-1 Hongo, Bunkyo-ku, Tokyo, 113-8656, Japan.

⁴Marine Core Research Institute, Kochi University, 200 Monobe Otsu, Nankoku, Kochi, 783-8502, Japan.

Corresponding author: Yasuhiro Kato (ykato@sys.t.u-tokyo.ac.jp) ORCID: 0000-0002-5711-8304

Key Points:

- Here, we report bulk $\delta^{13}\text{C}$, $\delta^{18}\text{O}$, and chemical compositions of early Paleogene sediments from Hole 762C in the Indian Ocean.
- We updated age model of Hole 762C by multiple Eocene hyperthermal horizons, indicated by the bulk $\delta^{13}\text{C}$ record.
- Independent component analysis on bulk compositions revealed Paleogene climate upheavals affected depositional environments at the site.

Abstract

The early Paleogene, including the Paleocene and Eocene, is characterized by Warmhouse and Hothouse climate states with superimposed transient warming events known as hyperthermals. While these paleoenvironmental changes are well-documented in the Pacific and Atlantic Oceans, records of such changes in the Indian Ocean are limited. Here, we present a new dataset of bulk chemical composition and stable isotopic ratios from the late Paleocene to middle Eocene sediments on the Exmouth Plateau in the mid-latitude eastern Indian Ocean. The bulk $\delta^{13}\text{C}$ and $\delta^{18}\text{O}$ suggest a warming period called the Early Eocene Climatic Optimum (EECO) and cooling towards the middle Eocene in a long-term perspective. In the short-term, we identified at least six hyperthermals (PETM, H2, I1, J, ETM3, and L) in the studied sections. By applying independent component analyses (ICA) to the bulk chemical composition data, we identified six independent components (ICs) corresponding to sediment source materials and post-depositional processes. The ICA result infers an increase in detrital materials or a decrease in carbonate rain flux, and an increased population of higher-order consumers in the oceanic ecosystem during both long-term (EECO) and short-term (hyperthermal) warmings around the Exmouth Plateau. Furthermore, ICs representing diagenetic processes and post-depositional remobilization of elements showed excursions across the hyperthermal horizons, indicating that changes in the redox state of pore or bottom water are associated with hyperthermals. This study provides critical insights into the paleoceanography of the Indian Ocean, highlighting the response of marine environments to both long-term and short-term climatic events during the early Paleogene.

Plain Language Summary

This study examined marine sediments from the mid-latitude eastern Indian Ocean dating back to the early Paleogene period, approximately 57 to 40 million years ago. During this time, Earth's climate was much warmer than today, with several short-term warming events known as hyperthermals. By analyzing the stable carbon and oxygen isotope ratios and the bulk chemical composition of these sediments, we identified six distinct hyperthermals, including the Paleocene–Eocene Thermal Maximum (PETM), which was the severest global warming event among the early Paleogene hyperthermals. By applying a multivariate statistical method called independent component analysis to the bulk chemical composition dataset, we extracted geochemical features of sediments, including the contributions of source materials (detrital materials, biogenic materials), and signatures of post-depositional chemical processes. The analysis indicated that inputs of detrital materials from continents and populations of higher consumers in the ocean, such as fish, increased during both long- and short-term warmings. Additionally, several elements were remobilized within the sediment because of changes in the redox state of pore or bottom water. This research provides valuable insights into the link between past climate events and changes in ocean and sediment chemistry, helping us understand how warm periods shaped marine ecosystems and oceanic environments.

1 Introduction

Among the long-term climatic trends of the Cenozoic, the early Paleogene is a globally warm period. In the context of long-term ($\sim 10^6$ yr) Cenozoic climate trends, peak warmth occurred during the Early Eocene Climatic Optimum (EECO, 53.260–49.140 Ma; Westerhold et al., 2020; Zachos et al., 2001). During the EECO, the atmospheric $p\text{CO}_2$ levels were two or three times higher than those of the modern Earth, and several hypotheses, such as active volcanism

and CO₂ released by organic-rich material decomposition, have been proposed for the increased $p\text{CO}_2$ (Hodell et al., 2007; Kirtland Turner et al., 2014; Komar et al., 2013). After the EECO, the global climate cooled towards the middle Eocene. Superimposed on this million-year-long warm period during the late Paleocene–early Eocene were transient (10^4 – 10^5 yr) warming events called “hyperthermals” (Thomas, 1998; Westerhold et al., 2017). The most pronounced and well-studied hyperthermal event is the Paleocene–Eocene Thermal Maximum (PETM, 55.93 Ma), characterized by intense global warming (5–9 °C rise in sea surface temperature, SST) and ocean acidification associated with the negative carbon isotope ($\delta^{13}\text{C}$) excursion (CIE, e.g., Kennett & Stott, 1991; McInerney & Wing, 2011; Zachos et al., 2003, 2005). Potential triggers for PETM include massive volcanism, the collapse of seafloor methane hydrates, and the exhalation of thermogenic methane (Berndt et al., 2023; Dickens et al., 1995; Gutjahr et al., 2017; Svensen et al., 2004), though the ultimate cause remains debated. Other hyperthermals with negative CIEs, such as the Eocene Thermal Maximum 2 (ETM2), H2, I1, I2, J, and ETM3, have also been reported. Recently, Earth’s orbital pacing has been suggested to be a key factor in the occurrence of multiple hyperthermals (Westerhold et al., 2017). The background climate, referred to as Hothouse climate, and hyperthermals during the early Paleogene have garnered considerable attention as a paleo-analog to the potential fate of contemporary climate changes, including global warming.

The paleoceanographic environment during the early Paleogene has been deduced from geochemical records of seafloor sediments. One characteristic paleoceanographic change associated with warming is carbonate compensation depth (CCD) elevation. From a long-term perspective ($\sim 10^6$ yr), the CCD shallowed during the EECO (Pälike et al., 2012); however, from a short-term perspective ($\sim 10^5$ yr), further CCD shallowing also occurred at hyperthermals (e.g., Raffi & Bernardi, 2008; Slotnick et al., 2015; Zachos et al., 2005). The CCD shallowing corresponding to the long- and short-term warming has been attributed to the pH lowering of seawater due to high atmospheric $p\text{CO}_2$ (e.g., Anagnostou et al., 2016, 2020; Pälike et al., 2012; Zachos et al., 2005). The ocean stratification, acidification, and deep-water deoxygenation at hyperthermals, particularly in the PETM, have also been inferred by planktonic and benthic foraminiferal assemblages (e.g., Kaiho et al., 2006; Thomas, 1998), the enrichment/depletion of redox-sensitive-elements in the marine sediments (Chun et al., 2010; Pälike et al., 2014), and other novel geochemical proxies (e.g., I/Ca, $\delta^{238}\text{U}$; Clarkson et al., 2021; Zhou et al., 2016). In addition to PETM, perturbations in oceanic chemistry occurred during other hyperthermals (e.g., ETM2; Harper et al., 2020; D’haenens et al., 2014).

The Indian Ocean, the major seawater path between the Atlantic and the Pacific during the early Paleogene (Thomas et al., 2003), is important in elucidating paleoceanographic conditions during the early Paleogene in a global context. Geochemical investigations of Indian Ocean sediments can provide fundamental clues for evaluating global behavior in the early Paleogene Hothouse climate. Geochemical records of hyperthermals, especially of the PETM, from the Atlantic and Pacific Oceans have been well established (e.g., Cramer et al., 2003; Hollis et al., 2015; Lauretano et al., 2015; Leon-Rodriguez & Dickens, 2010; Littler et al., 2014; Lourens et al., 2005; Nicolo et al., 2007; Niederbockstruck et al., 2024; Stap et al., 2010; Westerhold et al., 2018), whereas records from the Indian Ocean are comparatively limited (Barnet et al., 2020; Slotnick et al., 2015; Tanaka et al., 2022; Tremolada & Bralower, 2004; Yasukawa et al., 2017).

In this context, we focused on the Ocean Drilling Program (ODP) Hole 762C from offshore of the northwestern margin of the Australian continent (Exmouth Plateau; Figure 1a). The ODP Scientific Results reported bulk carbonate $\delta^{13}\text{C}$ and $\delta^{18}\text{O}$ records from Hole 762C (Thomas et al., 1992) and roughly indicated the existence of multiple hyperthermals supported by paleomagnetic and biostratigraphic studies (Galbrun, 1992; Shamrock & Watkins, 2012; Shamrock et al., 2012). However, the temporal resolution of the reported $\delta^{13}\text{C}$ and $\delta^{18}\text{O}$ records was low, and hyperthermal horizons were not firmly determined. Here, we report higher resolution records of bulk $\delta^{13}\text{C}$ and $\delta^{18}\text{O}$ from the early Paleogene (late Paleocene–middle Eocene) section of Hole 762C, identify hyperthermal horizons, and show long-term $\delta^{13}\text{C}$ and $\delta^{18}\text{O}$ trends at the site. Further, based on the bulk $\delta^{13}\text{C}$ record, we revised the age model of the Hole 762C core.

In addition to the C and O isotopes, we analyzed the bulk chemical composition of the early Paleogene carbonate sediments of Hole 762C to discuss the paleoceanographic condition at the site in the Eocene. The bulk chemical composition of seafloor sediments reflects the mixed signals of each source material and post-depositional element redistribution (e.g., diagenesis, redistribution, and precipitation; Dunlea et al., 2015; Plank & Langumuir, 1998). However, applying conventional approaches based on the bivariate correlations among each element or normalized data is difficult when extracting and interpreting essential information from multi-element datasets. In particular, carbonate sediments are challenging to decipher source materials and post-depositional processes due to the strong dilution effect of biogenic CaCO_3 (e.g., Yasukawa et al., 2017). Thus, most previous studies on geochemical features use only representative elements' abundances, which inevitably exclude signatures underlying the high-dimensional, entire data structure.

To overcome these challenges, we applied independent component analysis (ICA), a type of multivariate statistical analysis, to extract geochemical signals hidden in multi-elemental data of the bulk chemical composition of Hole 762C sediments. ICA extracts features based on non-Gaussianity in a multivariate dataset and is considered an appropriate analytical method for geochemical data with a non-Gaussian data structure (e.g., Iwamori & Albarède, 2008; Yasukawa et al., 2016). A brief summary of the principles of ICA is provided in the Supporting Text S1. In recent years, ICA has been successfully applied to high-dimensional geochemical datasets, including the bulk chemical composition of seafloor sediments (Kato et al., 2011; Yasukawa et al., 2016, 2017, 2019). By applying ICA, the observed multidimensional dataset consisting of the concentration of each element could be transformed into the linear combination of base vectors (independent components: ICs) corresponding to the source materials and geochemical processes of the sediments. For detailed formulation on using ICA in marine sediment analysis, see Yasukawa et al. (2016). In this study, by applying ICA to the geochemical dataset, we evaluated the paleoceanographic changes at Hole 762C in the mid-latitude eastern Indian Ocean.

2 Geological Settings and Lithology

ODP Leg 122 Site 762 Hole C ($19^\circ 53.23'\text{S}$, $112^\circ 15.24'\text{E}$) is located on the central Exmouth Plateau in the Northern Carnarvon Basin, ~300 km offshore of the northwestern coast of the Australian continent. According to the paleogeographic reconstruction (Scotese, 2001), the Exmouth Plateau was located in the mid-latitude of the eastern margin of the Indian Ocean

157 during the early Paleogene (~60–40 Ma; Figure 1a). The Northern Carnarvon Basin was initially
158 formed by the stretching during the Carboniferous–Cretaceous, and the Exmouth plateau has
159 been thought to be inactive after the mid-Cretaceous (Bilal & McClay, 2022). Since then, the
160 Cenozoic sedimentary environment has corresponded to an open-ocean setting (Haq et al., 1992).
161 The present-day water depth of this site is 1360 m (Haq et al., 1990; Figure 1b), and the
162 paleodepth of the early Paleogene is comparable to that reported today (1000–1200 m; Haq et al.,
163 1992; Jones & Wonders, 1992).

164 The lithology of the early Paleogene section of Hole 762C mainly consists of nannofossil
165 chalk that was deposited above the CCD and has been divided into three lithologic subunits (Unit
166 II, Subunit IIIA, and Subunit IIIB; Haq et al., 1990; Shamrock et al., 2012). Unit II (181.5–265.0
167 meter(s) below seafloor, mbsf) consists of white consolidated nannofossil ooze/chalk deposited
168 during the middle Eocene to the early Oligocene. Subunit IIIA (265.0–398.0 mbsf) consists of
169 pale green–light green-grey nannofossil chalk with foraminifers deposited during the early–
170 middle Eocene. Subunit IIIB (398.0–554.8 mbsf) consists of light green-grey–white nannofossil
171 chalk deposited during the early Paleocene–early Eocene. Previous studies based on
172 magnetostratigraphy and biostratigraphy identified four hiatuses in the early Paleogene section of
173 Hole 762C (Hiatus A: 289.75 mbsf, Hiatus B: 321.13 mbsf, Hiatus C: 332.18 mbsf, Hiatus D:
174 412.75 mbsf; Shamrock et al., 2012).

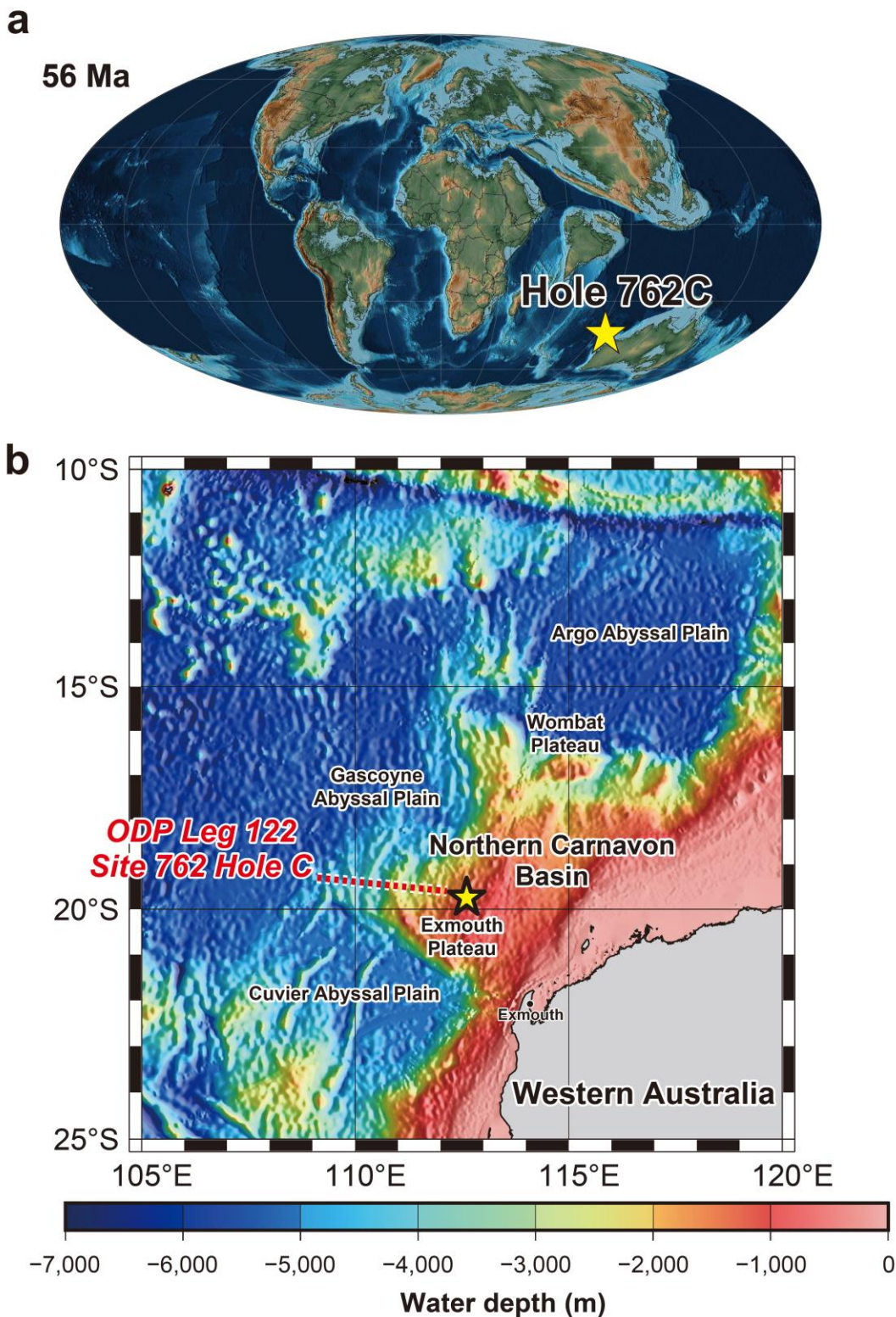


Figure 1. Location of the study site. (a) Paleogeographic reconstruction of the latest Paleocene (56 Ma) using data from Scotese (2001). Stars indicate the paleo-location of ODP Hole 762C. (b) Current location of the Exmouth Plateau and ODP Hole 762C. The bathymetry is based on 1 min gridded relief data by NOAA (ETOPO1; <https://www.ngdc.noaa.gov/mgg/global/global.html>).

3 Materials and Methods

3.1 Materials

We targeted 248 samples from the late Paleocene (Thanetian)–middle Eocene (Bartonian) section of Hole 762C, corresponding to lithologic Subunits IIIA and IIIB. The sampling resolution was 5–50 kyr for the latest Paleocene–early Eocene section, which was considered to record the PETM and early Eocene hyperthermals. We collected samples with >50 kyr intervals from other sections. All samples were collected from the working half, and the consolidated mud slurry between “biscuits” of actual sediments was carefully avoided.

As a result of the smear slide observations by shipboard scientists (Haq et al., 1990) and this study, the studied samples of Hole 762C mainly consist of calcareous nannofossils, which can be considered as fragments of coccolith (70–95%) and planktonic foraminiferal shells (2–30%). The contribution of detrital components (e.g., quartz, feldspar, and clay minerals) was minor (<5%). In addition, authigenic pyrite grains (100–200 μm) were observed at Core 28X (412.86–413.36 mbsf).

3.2 Carbon and Oxygen Stable Isotope Analyses

Before the geochemical analyses, bulk samples were dried in a vacuum freeze dryer (EYELA FDU-1200) and crushed by an agate mortar and pestle. After sample preparation, we conducted carbon ($\delta^{13}\text{C}$) and oxygen ($\delta^{18}\text{O}$) stable isotope analyses using GV Instruments IsoPrime with a dual-inlet system at the Center for Advanced Marine Core Research (present Marine Core Research Institute), Kochi University. Approximately 100 μg of pulverized bulk samples were dissolved in phosphoric acid at 90 $^{\circ}\text{C}$, and released CO_2 was injected into the mass spectrometer.

The measured isotopic ratios were converted from standard delta notation to Vienna Pee Dee Belemnite by analyzing IAEA-603 standard reference material ($\delta^{13}\text{C} = 2.460 \pm 0.010\text{‰}$, $\delta^{18}\text{O} = -2.370 \pm 0.040\text{‰}$; Assonov et al., 2020). We also measured $\delta^{13}\text{C}$ and $\delta^{18}\text{O}$ of geological reference carbonate materials (JCp-1) by the Geological Survey of Japan (GSJ) to evaluate analytical precision. In repeated analyses of IAEA-603 ($n = 60$) and JCp-1 ($n = 7$), the 2SE of $\delta^{13}\text{C}$ and $\delta^{18}\text{O}$ were less than $\pm 0.02\text{‰}$ and $\pm 0.04\text{‰}$, respectively.

3.3 Bulk Carbonate Analyses

The bulk carbonate content was determined using an elemental analyzer (Thermo Finnigan EA1112) installed at the Center for Advanced Marine Core Research (present Marine Core Research Institute), Kochi University. In this analysis, we assumed that the total inorganic carbon (TIC) of each sediment sample was incorporated as CaCO_3 , and TIC corresponds to the difference between total carbon (TC) and total organic carbon (TOC) contents. Therefore, we obtained bulk CaCO_3 content (wt.%) using the following equations:

$$[\text{TIC}] = [\text{TC}] - [\text{TOC}] \quad (1)$$

$$[\text{CaCO}_3] = [\text{TIC}] \times \frac{W_{\text{CaCO}_3}}{W_c} \quad (2)$$

where W_{CaCO_3} and W_C in equation (2) are the formula weight of CaCO_3 (100.0869) and the atomic weight of carbon (12.0107), respectively.

In the TC measurement, ~2 mg of bulk samples enclosed in tin capsules were introduced to the elemental analyzer and measured by a packed column. In TOC measurement, ~10 mg of bulk samples were digested by 100 μL of organic-free 3N HCl in silver capsules to remove CaCO_3 . After drying, the residues of the samples in silver capsules were overwrapped by tin capsules and introduced to the elemental analyzer. To make calibration curves, we simultaneously analyzed sulfanilamide standard reference materials.

3.4 Major- and Trace-element Analyses

The major- and trace-element content of bulk samples was determined by Thermo Fisher Scientific iCAP Q, an inductively coupled plasma quadrupole mass spectrometer (ICP-QMS) installed at the Department of Systems Innovation, School of Engineering, the University of Tokyo. Each sample was digested by $\text{HF-HNO}_3\text{-HClO}_4$ and aqua regia, following the established method described by Kato et al. (2005) and Yasukawa et al. (2020). Geological reference materials (JB-2, JB-3, and JMS-2) by GSJ were also prepared simultaneously to evaluate analytical accuracy.

In the ICP-QMS analyses, the difference between analyzed and published data of GSJ standards generally falls within 5%, except for Cr, As, and Ta (Supporting Table S1; Imai et al., 1995; Lu et al., 2007; Makishima & Nakamura, 2006; Yasukawa et al., 2020). The reproductivity of replicate analyses ($n = 8$) is basically within 5% relative standard deviation (RSD), except for As, Sb, and Ta, which sometimes result in larger than 20% RSD (Supporting Table S1).

3.5 Independent Component Analysis

In this study, we applied ICA to a 248×40 data matrix from Hole 762C; the rows corresponded to the individual bulk sediment samples, and the columns corresponded to the elements. The variables consist of the abundance of Mg, Al, P, K, Sc, Ti, V, Mn, Fe, Co, Ni, Cu, Zn, Rb, Sr, Y, Zr, Nb, Mo, Cs, Ba, La, Ce, Pr, Nd, Sm, Eu, Gd, Tb, Dy, Ho, Er, Tm, Yb, Lu, Hf, Pb, Th, U, and CaCO_3 . Sodium content was not included in the matrix because saline could largely affect Na content (Yasukawa et al., 2016). Contents of Cr, As, Sb, and Ta were not included in the ICA because these elements show large RSDs through the analytical batches and large differences (>20%) from published data for standard materials. Before calculation, the dataset was centered with each variable's mean set to zero, made uncorrelated using a conventional principal component analysis algorithm, and scaled to have unit variance along each principal component. The computation of the ICA for our dataset was implemented using the open R package “FastICA” originally released by Marchini et al. (2013), with some modifications by Yasukawa et al. (2016, 2023). The R script is in Kuwahara et al. (2024a)

In performing ICA, we determined the number of ICs and applied the “Guttman–Kaiser criterion (Guttman, 1954; Kaiser, 1960)” to the eigenvalues obtained from the principal component analysis algorithm (Supporting Text S2). Our analysis revealed that the eigenvalues of the first six principal components (PCs 1–6) were greater than unity, and these six components accounted for 87.9% of the total sample variance (Supporting Figure S1; Table S2).

After performing ICA, the results were interpreted based on the relative (i.e., variance-normalized) IC loadings and IC scores. The relative IC loadings denote the contributions of each element to the individual ICs. A large loading indicates a strong correlation between the element concentration and the respective IC. As another output of ICA, the IC score represents the coordinate values of sample data projected into the linear space spanned by IC vectors. In simpler terms, IC scores quantify the intensities of each independent source signal in each sample.

4 Results

4.1 Carbon and Oxygen Stable Isotope Ratios

The analytical data of bulk carbonate $\delta^{13}\text{C}$ and $\delta^{18}\text{O}$ of Hole 762C samples are shown in Supporting Table S3. Depth profiles of $\delta^{13}\text{C}$ and $\delta^{18}\text{O}$ at Hole 762C are shown in Figure 2a. In the overall trend from Core 29X to Core 12X, bulk $\delta^{13}\text{C}$ values were $\sim 3\text{‰}$ during 425–413 mbsf and dropped to $\sim 2\text{‰}$ at ~ 413 mbsf. Thereafter, between 395 to 340 mbsf, the $\delta^{13}\text{C}$ values gradually decreased to $\sim 0\text{‰}$. The bulk $\delta^{18}\text{O}$ generally started around -1.0‰ between 425 and 340 mbsf and increased to 0.0‰ during 340–307 mbsf. Afterward, bulk $\delta^{18}\text{O}$ rose gradually at depths shallower than 280 mbsf and reached $\sim 0.5\text{‰}$ at 265 mbsf.

We found five distinct negative excursions of the bulk $\delta^{13}\text{C}$ in Core 25X–22X (Figure 3b). In these cores, bulk $\delta^{18}\text{O}$ also shows negative excursions associated with those of $\delta^{13}\text{C}$, although the $\delta^{18}\text{O}$ fluctuates throughout the section. The magnitude of the five excursions of $\delta^{13}\text{C}$ (difference between excursion peak and onset) at 395, 390, 379, 373, and 366 mbsf are -0.6‰ , -0.7‰ , -0.5‰ , -0.9‰ , and -0.4‰ respectively. Conversely, the magnitudes of $\delta^{18}\text{O}$ excursions at each horizon are -0.5‰ , -0.2‰ , -0.3‰ , -0.4‰ , and -0.1‰ respectively. In addition, several smaller-scale negative excursions of $\delta^{13}\text{C}$ ($\sim -0.4\text{‰}$) and $\delta^{18}\text{O}$ ($\sim -0.2\text{‰}$) are also observed in Core 21X–18X (Figure 2a). In contrast, no noticeable negative $\delta^{13}\text{C}$ excursion was observed in Core 14X–12X, corresponding to the middle Eocene period.

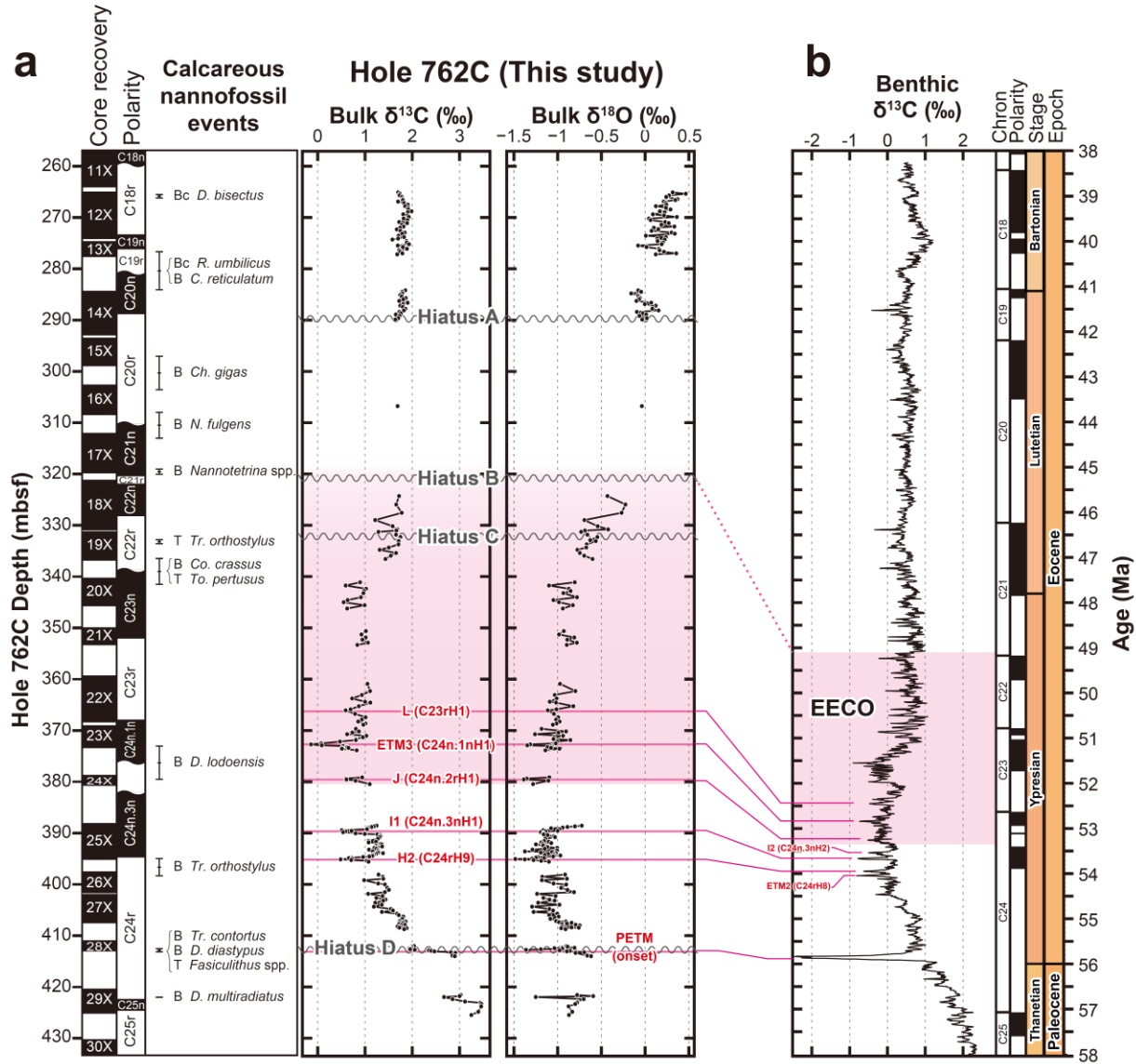


Figure 2. Correlation between (a) bulk $\delta^{13}\text{C}$ and $\delta^{18}\text{O}$ data from ODP Hole 762C and (b) the reference benthic $\delta^{13}\text{C}$ profile (Westerhold et al., 2020). Magnetostratigraphic (Galbrun, 1992; Shamrock et al., 2012), and calcareous nannofossil events (Shamrock & Watkins, 2012) at Hole 762C are also shown in panel (a). The analytical uncertainties of bulk $\delta^{13}\text{C}$ and $\delta^{18}\text{O}$ of Hole 762C were less than 0.02‰ and 0.04‰, respectively. Note for calcareous nannofossil events: B = Base, T = Top, Bc = Base common occurrence. The waved lines indicate the four hiatuses identified by Shamrock et al. (2012).

4.2 Bulk chemical compositions

The bulk chemical composition data of Hole 762C, including TC, TOC, and CaCO_3 contents, are shown in Supporting Table S4. The results show that Ca is the most abundant element in the samples of Hole 762C ($\text{Ca} = 23.7\text{--}38.9$ wt.%), and CaCO_3 accounts for 60.2–93.3 wt.% of bulk samples. Among the other major elements, Fe and Al are contained in percent order ($\text{Al} = 0.297\text{--}2.23$ wt.%; $\text{Fe} = 0.180\text{--}2.13$ wt.%). In the trace element composition (elements in the order of ppm), Sr and Ba show considerably high concentrations ($\text{Sr} = 580\text{--}1308$ ppm; $\text{Ba} = 366\text{--}1683$ ppm) compared to other trace elements.

In the depth profile of each element, the concentration of CaCO_3 , the most abundant component in the studied samples, dropped at the horizons of negative $\delta^{13}\text{C}$ and $\delta^{18}\text{O}$ excursions (395, 390, 379, and 373 mbsf; Figure 3b, c). In addition, the CaCO_3 abundance also dropped at 422, 373, and 288 mbsf (Supporting Figure S4a). Conversely, depth profiles of detrital-origin elements (e.g., Ti, Al) are correspondingly symmetric to that of CaCO_3 (Supporting Figure S5). The depth profiles of P, Y, and total rare earth elements (REEs; here indicating from La to Lu) were similar and showed sharp peaks at 404, 373, and 331 mbsf. Some metal elements (e.g., Cu, Pb) showed several spike-like peaks in the depth profiles (Supporting Figure S5). Except for each peak, these elements generally showed relatively less variable profiles in the long-term trend.

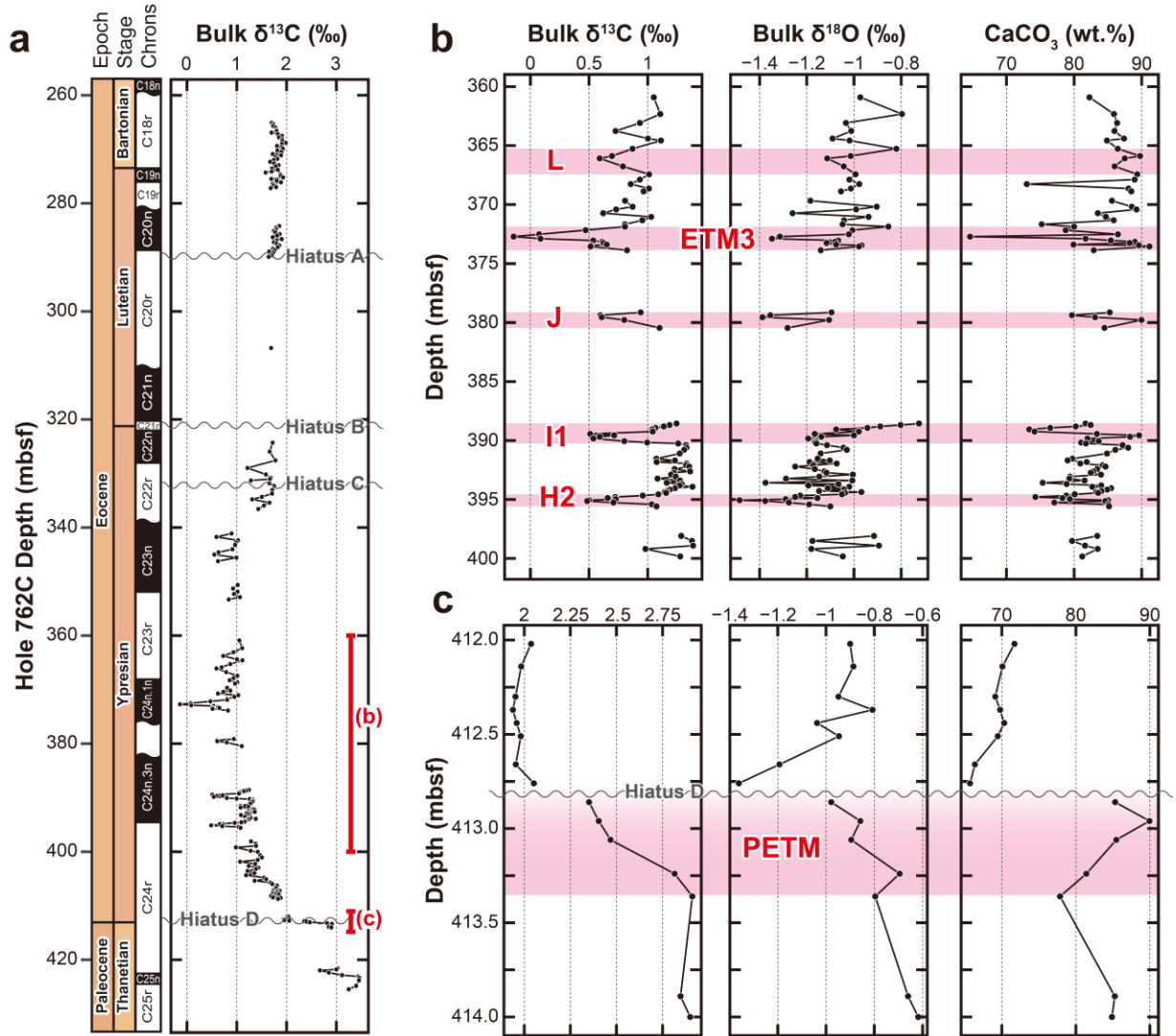


Figure 3. Depth profiles of bulk $\delta^{13}\text{C}$, $\delta^{18}\text{O}$, and CaCO_3 of Hole 762C. (a) All data. (b) Data from early Eocene (Core 25X–22X). (c) Data around Paleocene–Eocene boundary (Core 28X). Intervals with red lines indicate ranges of panels (b) and (c). Analytical uncertainties of $\delta^{13}\text{C}$ and $\delta^{18}\text{O}$ are less than 0.02‰ and 0.04‰, respectively. In panel (a), magnetostratigraphic columns and identified hiatuses are also shown (Shamrock et al., 2012).

4.3 Independent Component Analysis

In this study, we implemented ICA on a dataset consisting of 40 elements and 248 samples from Hole 762C. The relative IC loadings are presented in Figure 4. It should be noted that the numbering of ICs is arbitrary and commutative and does not indicate their mutual importance. The scatterplots depicting the relationships between ICs indicate clear orthogonality among the six components in the IC space, demonstrating their statistical independence from one

329 another (Supporting Figure S6). The validity of extracting six ICs is discussed on Supporting
330 Text S2 in detail. Our subsequent discussion is based on the results corresponding to the six ICs
331 (Figure 4).

332

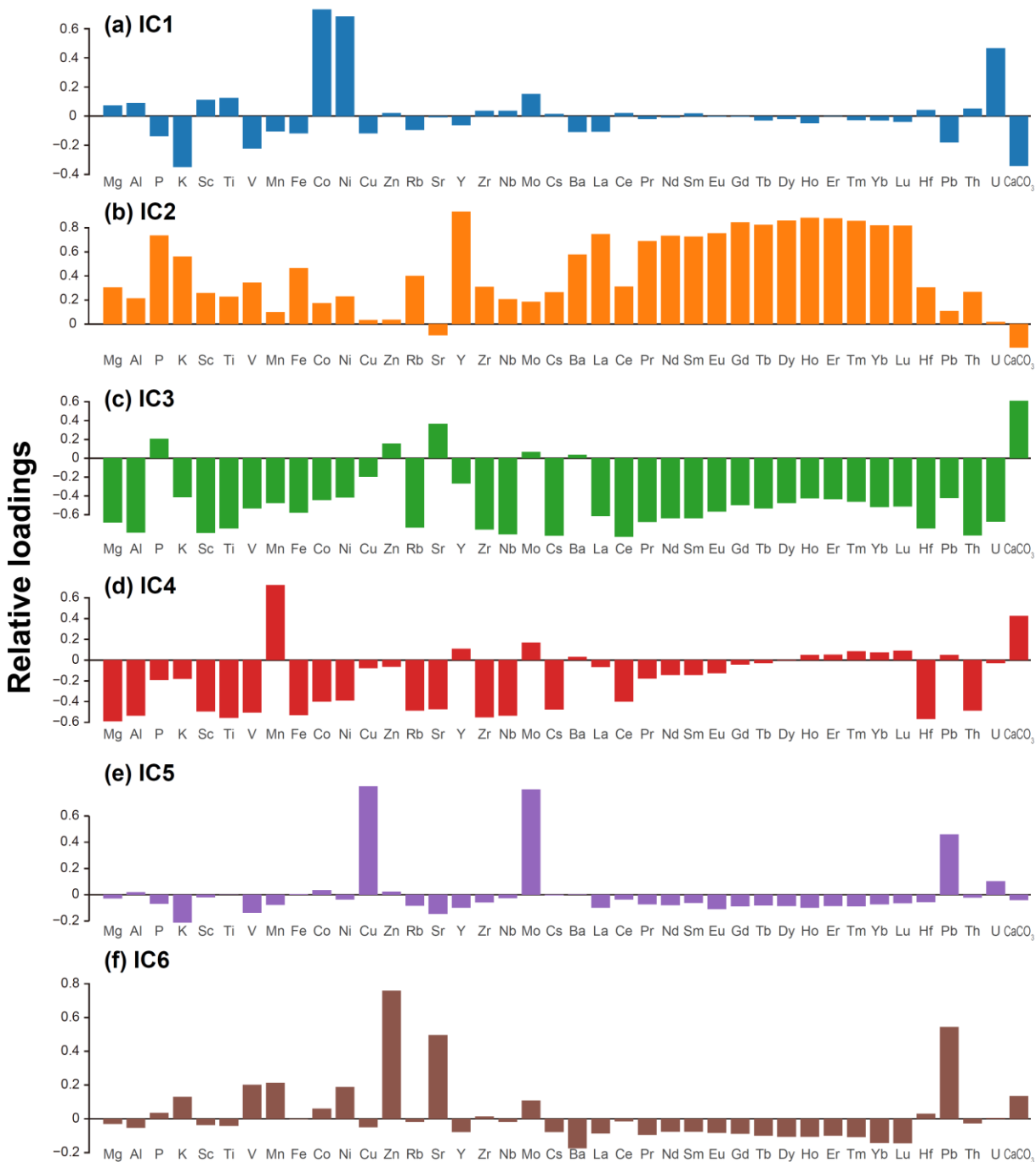


Figure 4. IC loadings of major and trace elements obtained from the Hole 762C dataset when the number of ICs = 6.

5 Discussion

5.1 Identification of Hyperthermals and Revision of the Age Model

Although previous studies have suggested that Hole 762C sediments contain multiple hyperthermal horizons (Shamrock et al., 2012; Thomas, 1992; Xu et al., 2021), the precise identification of hyperthermal events has not been achieved owing to the limited temporal resolution of previous bulk $\delta^{13}\text{C}$ and $\delta^{18}\text{O}$ records and coring gaps. Thus, the age model of Hole 762C must be further considered. In this study, we identified the hyperthermal horizons of Hole 762C using the newly obtained bulk carbonate $\delta^{13}\text{C}$ and $\delta^{18}\text{O}$ records in combination with the age constraints by magnetostratigraphy and biostratigraphy of Hole 762C (Galbrun, 1992; Shamrock & Watkins, 2012; Shamrock et al., 2012; Figure 2a) and the astronomically tuned compilation of benthic foraminifera $\delta^{13}\text{C}$ records “CENOGRID” (Westerhold et al., 2017, 2018, 2020; Figure 2b).

Although poor coring recovery and strong disturbance of Core 28X of Hole 762C complicate the interpretation of the hyperthermal horizon, we identified the onset of the PETM in Core 28X as the drop in bulk $\delta^{13}\text{C}$ from 2.91‰ at 413.36 mbsf to 2.35‰ at 412.86 mbsf (Figure 3c). This section was previously identified as the PETM horizon based on the negative $\delta^{13}\text{C}$ excursion of the bulk carbonate (Thomas et al., 1992). The drastic change in the calcareous nannofossil assemblage between 413.25 mbsf (NP9, CP8a; e.g., *Discoaster multiradiatus*; *Fasiculithus* spp.) and 412.59 mbsf (NP10, CP9a; e.g., *Tribrachiatus contortus*; *Discoaster diastypus*) also supports this interpretation (Supporting Figure S7; Shamrock et al., 2012).

However, the lack of the CP9b zone and the discontinuity in the core facies at 412.78 mbsf and bulk $\delta^{13}\text{C}$ only show a stepwise decrease ($\sim 0.6\text{‰}$) without an evident peak indicating the occurrence of a hiatus or truncation of the PETM horizon at Hole 762C (Shamrock et al., 2012; Supporting Figure S7). As we did not observe a clay-rich layer near the PETM horizon, the lack of a PETM peak and CP9b zone in the Hole 762C sediments could be explained by a hiatus and/or physical erosion rather than carbonate dissolution (truncation) associated with the shallowing of the CCD, as observed in some PETM horizons from other locations (e.g., Raffi & Bernardi, 2008; Zachos et al., 2005). Based on these observations, we interpret that while the onset of the PETM was recorded between 413.36–412.86 mbsf, the body and recovery periods of the PETM are lacking in Hole 762C. We assigned 413.36 mbsf at Hole 762C, where the decline in bulk $\delta^{13}\text{C}$ begins, as the age of the PETM onset (Figure 2; 55.930 Ma; Westerhold et al., 2017, 2018).

Regarding the younger, early Eocene hyperthermals, the CIE ($\sim 0.6\text{‰}$) at 389.44 mbsf in Core 25X occurs at the latest magnetochron C24r (Figure 3), which is known to contain two hyperthermal events, namely the ETM2 (C24rH8) and H2 Event (C24rH9) (Figure 2b; Westerhold et al., 2017). Previous studies based on bulk carbonate $\delta^{13}\text{C}$ data by Thomas (1992) identified this CIE as ETM2 (Shamrock et al., 2012; Shamrock & Watkins, 2012). If this interpretation is correct, another CIE corresponding to the H2 Event should be present immediately after the CIE at 389.44 mbsf. However, our newly obtained bulk carbonate $\delta^{13}\text{C}$ record does not show such a CIE in the magnetochron C24r interval. Therefore, we interpret that

the CIE at 389.44 mbsf corresponds to the H2 Event rather than ETM2 (Figure 2; 53.950 Ma; Westerhold et al., 2017). Based on this interpretation, the horizon of ETM2 could have been lost due to the coring gap of the sediment.

A CIE ($\sim 0.7\%$) at 395.13 mbsf occurred in the obvious normal polarity interval in Core 25X, denoted as magnetochron C24n.3n (Figure 3). This CIE has not been reported in previous studies on Hole 762C. According to Westerhold et al. (2017), two hyperthermal events, I1 (C24n.3nH1) and I2 (C24n.3nH2), occurred during the magnetochron C24n.3n (Figure 2a). If this CIE corresponded to the I2 Event, another CIE corresponding to the I1 Event should have occurred immediately before this CIE at 395.13 mbsf. However, no equivalent CIE was observed in our bulk $\delta^{13}\text{C}$ record. Therefore, we interpret the CIE at 395.13 mbsf to correspond to the I1 Event (Figure 2; 53.665 Ma; Westerhold et al., 2018) and that the horizon of the I2 Event is missing due to the coring gap.

A small CIE ($\sim 0.5\%$) at 379.38 mbsf in Core 24X occurred during a transient reversed polarity phase in magnetochron C24n (i.e., C24n.2r). This CIE has not been previously reported in studies on Hole 762C. Although it is not conclusive due to poor core recovery of Core 24X, as only the J Event (C24n.2rH1) is currently reported during the magnetochron C24n.2r, we consider the CIE at 379.38 mbsf to correspond to the J Event (53.260 Ma; Westerhold et al., 2017).

The largest CIE ($\sim 0.9\%$) observed at Hole 762C was at 379.38 mbsf in Core 23X. This CIE occurred in the normal polarity phase of upper magnetochron C24n (i.e., C24n.1n) and above the base of *Discoaster lodoensis* nannofossil event (Shamrock et al., 2012; Shamrock & Watkins, 2012). The only hyperthermal event that satisfies all the above chronological constraints is considered to be ETM3 (K Event; C24n.1nH1), and we identified the 379.38 mbsf CIE as ETM3 (52.845 Ma; Westerhold et al., 2017), consistent with the interpretation by a previous study (Shamrock et al., 2012).

Two small CIEs ($\sim 0.4\%$) at 366.08 and 363.76 mbsf in Core 22X occurred above the base of magnetochron C23r (Figure 2). The two successive CIEs at the early stage of C23r were also reported by benthic and bulk $\delta^{13}\text{C}$ records by Westerhold et al. (2017) and identified as L Event (C23rH1). Due to the consistency in magneto-chemostratigraphic evidence, we interpret the former CIE at 366.08 mbsf at Hole 762C as the L Event.

Consequently, we identified at least six hyperthermals (PETM, H2, I1, J, ETM3, and L) in the latest Paleocene (Thanetian) to early Eocene (Ypresian) interval of Hole 762C (Figure 2a). Compared with other marine and terrestrial records of the bulk carbonate $\delta^{13}\text{C}$ record of hyperthermal events (excluding the PETM), the CIEs bulk carbonate $\delta^{13}\text{C}$ at Hole 762C exhibited generally consistent behavior and magnitude with records from the Atlantic, Pacific, and Indian Oceans (Supporting Text S3; Figure S8). Therefore, despite the occurrence of the coring disturbance, the geochemical records of five hyperthermals (H2, I1, J, ETM3, and L) at Hole 762C are complete without hiatus or truncation.

Previous studies have suggested that the Middle Eocene Climatic Optimum (MECO) horizon exists in Cores 12X and 13X (284.0–265.0 mbsf), the uppermost part of the studied section of Hole 762C, based on the nannofossil assemblages (Shamrock et al., 2012). The MECO,

a one-million-year warming event, is marked by a positive $\delta^{13}\text{C}$ anomaly and a negative $\delta^{18}\text{O}$ anomaly (e.g., Bohaty & Zachos, 2003; Rivero-Cuesta et al., 2019). However, these anomalies were not clearly observed in bulk $\delta^{13}\text{C}$ and $\delta^{18}\text{O}$ records of Cores 12X and 13X of Hole 762C. Thomas et al. (1992) observed an increase in bulk $\delta^{13}\text{C}$ and a decrease in bulk $\delta^{18}\text{O}$ (2.41‰ and -0.05‰, respectively) in Core 11X (260.71 mbsf; Supporting Figure S9). Along with the base common occurrence of *Dictyococcites bisectus* (265.51 mbsf), which marks the beginning of the MECO (Shamrock and Watkins, 2012), we interpret that Hole 762C Core 12X corresponds to the interval before MECO onset. Consequently, we compared the bulk $\delta^{13}\text{C}$ record of Hole 762C to other MECO horizons from Atlantic and Southern Ocean sites (Holes 702B, 738B, Site 1263; Rivero-Cuesta et al., 2019, and references therein), and placed age tie points at peak and end of a weak bulk $\delta^{13}\text{C}$ increase during C18r, before the onset of MECO (Supporting Figure S9, Table S5). This age correlation has large uncertainties, and further stable isotope data of Core 11X are needed to identify the MECO horizon and construct a more reliable age model for the middle Eocene interval of Hole 762C.

Based on the age determination in this study, the depositional ages of studied samples from Hole 762C were estimated to be from 57.65 Ma (Late Paleocene: Thanetian) to 40.67 Ma (Middle Eocene: Bartonian; Figure 5). Based on the revised age model, the sedimentation rate at Hole 762C was calculated to be 0.37–4.44 cm/kyr (Supporting Figure S10: Table S5), which is not significantly different from those reported by the previous study (0.57–3.57 cm/kyr; Shamrock et al., 2012). Hereafter, we discuss the time-series variations of geochemical signatures at Hole 762C with the revised age model.

5.2 Long-term Variation of Bulk Carbonate $\delta^{13}\text{C}$ and $\delta^{18}\text{O}$ Records

The bulk carbonate $\delta^{13}\text{C}$ of sediments reflects the $\delta^{13}\text{C}$ of dissolved inorganic carbon in seawater incorporated into the CaCO_3 (Luciani et al., 2016). As the studied samples from Hole 762C are nannofossil chalks mainly consisting of the coccoliths of calcareous phytoplankton and a small amount of planktonic foraminifera shells (Haq et al., 1990), the bulk carbonate $\delta^{13}\text{C}$ record of Hole 762C can be interpreted as the $\delta^{13}\text{C}$ of near-surface seawater (Thomas et al., 1992).

The bulk carbonate $\delta^{13}\text{C}$ values from Hole 762C generally matched those from the Atlantic (ODP Sites 1258, 1262, 1263, 1265, and 1267; Westerhold et al., 2017) and Indian Oceans (ODP Hole 758A and IODP Hole U1443A; Barnet et al., 2020); thus, the long-term variation in bulk $\delta^{13}\text{C}$ values of Hole 762C is likely to reflect a global trend (Figure 5a). In particular, the consistency between bulk $\delta^{13}\text{C}$ records at Hole 762C and Holes 758A/U1443A indicates that the bulk $\delta^{13}\text{C}$ of Hole 762C represents a reasonable dissolved inorganic carbon's $\delta^{13}\text{C}$ of the mixed layer in the Indian Ocean. In addition, a comparison of the long-term trends of the bulk carbonate $\delta^{13}\text{C}$ records of Hole 762C with the global compilation of $\delta^{13}\text{C}$ records of benthic foraminifera (CENOGRID; Westerhold et al., 2020), which reflects the $\delta^{13}\text{C}$ of deep seawater, revealed that the bulk carbonate $\delta^{13}\text{C}$ records of Hole 762C were ~1‰ higher than those of benthic $\delta^{13}\text{C}$ records throughout the studied period (late Paleocene to middle Eocene; Figure 5a). These features reflect that the ocean surface layer exhibits higher $\delta^{13}\text{C}$ than the deeper layers, which may indicate that deep seawater contains a larger amount of isotopically

light carbon derived from the decomposition of organic matter than near-surface seawater (Ravizza & Zachos, 2014).

The long-term decrease of bulk $\delta^{13}\text{C}$ records of Hole 762C from ~57.5 Ma (~3.3‰) to ~53.0 Ma (~0.0‰), as seen in Atlantic bulk $\delta^{13}\text{C}$ records and CENOGRID benthic $\delta^{13}\text{C}$ records, could be interpreted as the long-term increase in the net release of isotopically light carbon to the ocean (e.g., Kirtland Turner et al., 2014; Komar et al., 2013). Among several explanations for the $\delta^{13}\text{C}$ decrease proposed by previous studies, one of the leading hypotheses is the continuous release of carbon due to the decomposition of organic matter (e.g., biogenic CH_4 , permafrost, and peat) triggered by the orbital pacing (e.g., Barnett et al., 2019; Kirtland Turner et al., 2014; Komar et al., 2013). Our data indicate that the $\delta^{13}\text{C}$ decrease toward ~53 Ma is also a common phenomenon on the surface of the eastern Indian Ocean.

A ~1‰ increase in the bulk carbonate $\delta^{13}\text{C}$ during the magnetic polarity Chron C23n (52–51 Ma) was recognized at Hole 762C, albeit an incomplete record due to coring gap (Figure 5a). This $\delta^{13}\text{C}$ shift is commonly observed in global bulk and benthic $\delta^{13}\text{C}$ data (Westerhold et al., 2017, 2020). To date, several debatable hypotheses, including increased carbon burial flux, changes in oceanographic circulation patterns, and active volcanism, attempt to explain the rise of $\delta^{13}\text{C}$ during C23n (Anagnostou et al., 2020; Westerhold et al., 2018). A global-scale upheaval of the terrestrial environment (e.g., temperature, precipitation rate; Hyland et al., 2017; Hyland & Sheldon, 2013) and tectonic events, including the change of the orientation of plate motion and generation of new subduction zone (e.g., Ishizuka et al., 2011; O'Connor et al., 2013; Whittaker et al., 2007) have been reported during Chron C23. These tectonic or environmental changes could contribute to changes in the global carbon cycle involving the rise of seawater $\delta^{13}\text{C}$.

During 50–41 Ma, the $\delta^{13}\text{C}$ record did not show long-term changes, indicating the absence of long-term changes in the carbon cycle. While previous studies reported the increase in $\delta^{13}\text{C}$ during 40.5–39.5 Ma known as MECO (Bohaty & Zachos 2003; Rivero-Cuesta et al., 2019; Westerhold et al., 2020), our Hole 762C cores did not show such an increase in $\delta^{13}\text{C}$ record, because our studied sections seem to be below the MECO horizon.

Bulk carbonate $\delta^{18}\text{O}$ values of well-preserved nannofossil chalk are generally considered to reflect SST, but they are strongly affected by recrystallization and/or the contribution of other components. In the case of Hole 762C, the lithology is dominated by calcareous nannofossils, with relatively good preservation throughout the Eocene interval (Siesser & Bralower, 1992). Thus, the bulk carbonate $\delta^{18}\text{O}$ of Hole 762C likely reflects a long-term SST trend in the mid-latitude eastern Indian Ocean. The long-term variation of bulk $\delta^{18}\text{O}$ at Hole 762C shows a gradual decrease from ~57.5 Ma (~−0.7‰) to ~52.5 Ma (~−1.3‰), and increase until ~46 Ma (~0.0‰). This secular variation of bulk $\delta^{18}\text{O}$ can be interpreted as an increase in SST toward the beginning of the EECO, followed by cooling towards the middle Eocene (Figure 5b). A slight increase in bulk $\delta^{18}\text{O}$ during 41.2–40.7 Ma may indicate SST cooling before the onset of the MECO (~40.6 Ma; Rivero-Cuesta et al., 2019).

The gap between the bulk $\delta^{18}\text{O}$ of Hole 762C and the globally compiled benthic $\delta^{18}\text{O}$ (Westerhold et al., 2020) narrowed during 54–50 Ma (Figure 5b). Although we cannot rule out the possibility of diagenetic effects and age uncertainty in the Hole 762C bulk $\delta^{18}\text{O}$ record, an

interpretation of this feature at Hole 762C is a decrease in the vertical gradient of temperature and density in the water column after 54 Ma. The convergence of water temperature between surface and intermediate-deep seawater is also suggested by $\delta^{18}\text{O}$ and Mg/Ca records from the Southern (ODP Sites 690 and 738; Auderset et al., 2022), Atlantic (DSDP Site 550; Charisi & Schmitz, 1996), Pacific (ODP Site 1209; Dutton et al., 2005), and low-latitude Indian Oceans (IODP Site U1443 and ODP Site 758; Barnett et al., 2020). Therefore, our bulk $\delta^{18}\text{O}$ data may imply the occurrence of a collapse of the vertical structure of the water column in the Exmouth Plateau. We cannot verify this interpretation at this stage, but stable isotope analyses of planktonic and benthic foraminifera shells of Hole 762C are expected to validate our hypothesis.

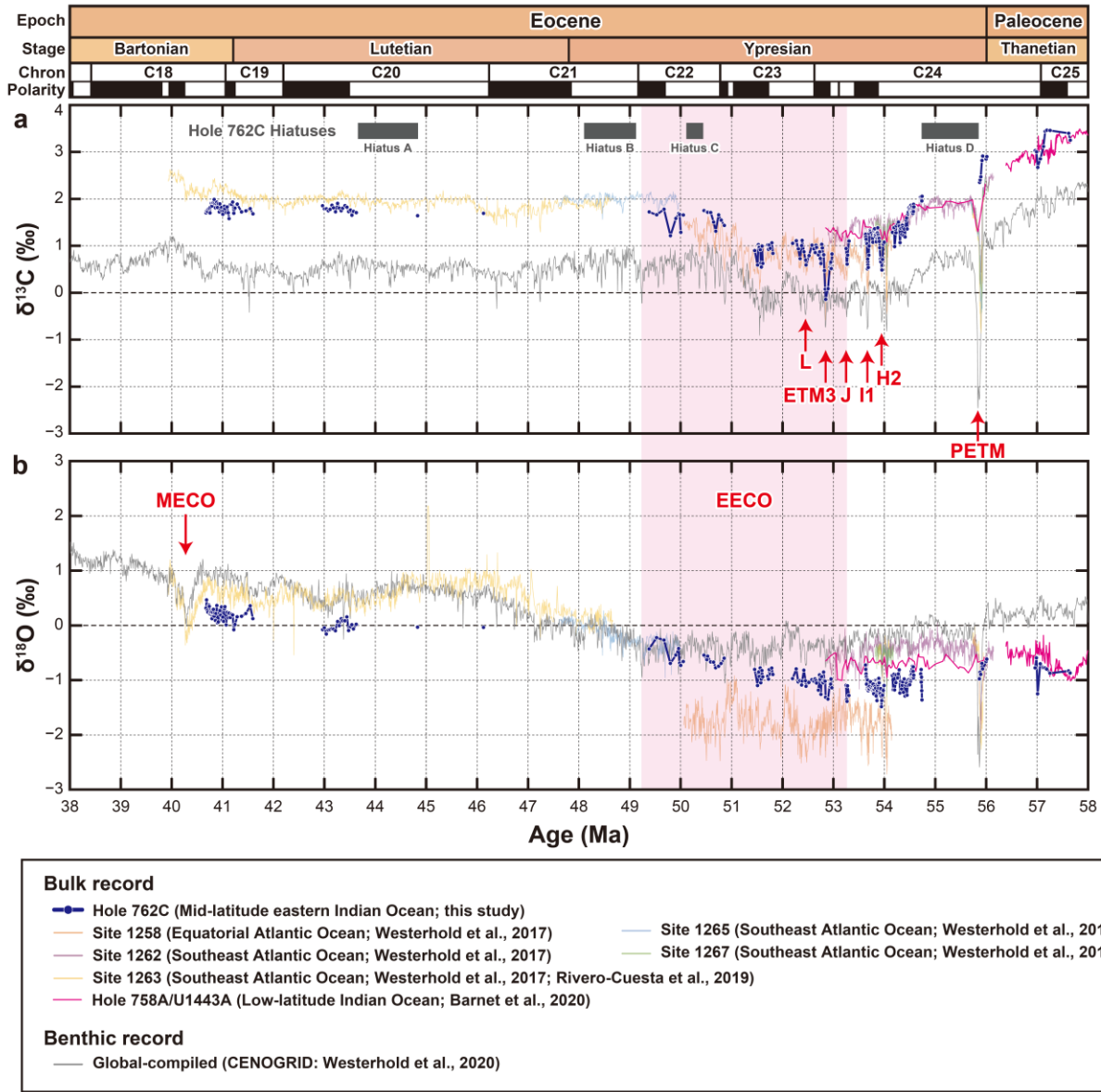


Figure 5. Late Paleocene to middle Eocene bulk carbon and oxygen stable isotope records from Hole 762C (this study) and previously reported bulk and benthic stable isotope records (Barnet et al., 2020; Rivero-Cuesta et al., 2019; Westerhold et al., 2017, 2020). Vertical red arrows indicate hyperthermals and MECO. Ranges of hiatuses at Hole 762C are also shown.

5.3 Long-term Variation of Geochemical Signature Based on ICA

As a result of the ICA for the bulk chemical composition of Hole 762C, we extracted six ICs (IC1–IC6). Based on the loadings of the elemental composition of each IC, we interpreted the geochemical components as follows: a mixing relationship between biogenic CaCO_3 and detrital components (IC3), biogenic calcium phosphate (IC2), diagenetic signature on carbonate (IC4), and redox-related behaviors of metal elements (IC1, IC5, and IC6). Detailed descriptions and interpretations of each IC are presented in Supporting Text S4. In this section, we discuss the long-term trends of geochemical signatures based on ICs throughout the studied section (IC2, IC3, and IC4).

5.3.1 Change of CaCO_3 Contribution Associated with Long-Term Climate Changes (IC3)

IC3 was characterized by positive CaCO_3 and Sr loadings and negative loadings of most other elements contained in detrital materials (e.g., Mg, Al, Ti, Sc, Rb, Zr, Nb, Cs, Hf, Th; Figure 4c). Therefore, we interpret that IC3 reflects the mixing relationship between biogenic CaCO_3 and detrital components. As the location of Hole 762C is a passive margin without a large change in paleogeography (especially the distance to the continent), and its paleodepth was generally constant throughout the Cenozoic (1000–1200 m; Haq et al., 1992; Jones & Wonders, 1992; Scotese, 2001; Figure 1a), neither the changes in water depth nor tectonic settings contributed to the changes in the abundance of biogenic CaCO_3 and detrital input to Hole 762C. Therefore, we considered that climatic or oceanographic changes mainly caused the variation in the IC3 scores.

Over the long term, changes in the IC3 score may be related to climatic changes in the mid-latitude eastern Indian Ocean. During 54.5–51.8 Ma, the IC3 score was negative, indicating relatively low biogenic CaCO_3 and high detrital content during the warm period, as indicated by bulk $\delta^{18}\text{O}$, at this site (Figure 6). The long-term variation in IC3 score can be explained by two scenarios. The first scenario involves long-term variation in the fluctuation of the depositional rate of CaCO_3 associated with the early Paleogene climate. Paleo-CCD estimation from the Pacific and Indian Oceans suggest that shallowing of CCD occurred under high ($\sim 1,100$ – $3,000$ ppmv) atmospheric $p\text{CO}_2$ and low pH seawater during the EECO (Anagnostou et al., 2016; Pálike et al., 2012; Slotnick et al., 2015). The emplacement of the hiatus after PETM onset (Hiatus D: 55.87–54.74 Ma; Supplementary Figure S7) may indicate a low CaCO_3 flux and/or physical erosion in the depositional area. A low sedimentation rate after PETM is also recorded from the low-latitude Indian Ocean (IODP Hole U1443A; Barnet et al. 2020), indicating that the seafloor environment after PETM in the Indian Ocean may not be suited for the deposit of carbonate sediments. However, the secular variation in the mass accumulation rates (MAR) of CaCO_3 during 54.5–51.8 Ma showed a high value (~ 1 g/cm²/kyr; Figure 6), suggesting that a reduced flux of carbonate deposition to the seafloor is not a major cause of the low IC3 score during 54.5–51.8 Ma.

Another more likely scenario explaining the low IC3 score (< 0) during 54.5–51.8 Ma is the increase in the influx of terrigenous material relative to CaCO_3 . Under the warm climate and enhanced hydrological cycle during the early Eocene, the supply of terrigenous materials into

the ocean has been suggested to be accelerated (e.g., Dallanave et al., 2015; Hyland and Sheldon, 2013). Therefore, a high contribution of terrigenous input at the Exmouth Plateau may have caused the negative (i.e., detrital-rich) value of the IC3 score during ~54.5–51.8 Ma. This interpretation is supported by the MAR of Al, which shows a high value (~60 mg/cm²/kyr) at ~54 Ma, followed by a decrease toward ~50 Ma (Figure 6). This trend is a mirror image of the IC3 score; thus, the long-term variation in the IC3 score is mainly controlled by terrigenous influx to Hole 762C.

As the major source of aeolian dust at the Exmouth Plateau after the Neogene is inland arid areas of northwestern Australia (Hasse & McTainsh, 2003; Le Houedec et al., 2012), the aeolian dust source at Hole 762C during the early Eocene could also be Australia. However, during the early Eocene, the terrestrial environment of northwestern Australia was considered to be warmer and wetter than that of the present (Martin, 2006; Reichgelt et al., 2022); thus, the dust flux from this region would have been smaller than that of current day. Therefore, it is unlikely that the increased aeolian dust flux caused an increase in terrigenous input under a warm climate of the early Eocene. In contrast, it has been reported that the contribution of terrigenous fluvial input into the deep-sea sediments around the continent has increased during the earliest Eocene and EECO (Burton et al., 2023). Thus, enhanced denudation, drainage, and chemical weathering in the warm and humid terrestrial environment in the early Eocene may have caused an increase in the riverine input of terrigenous materials to the coastal area and, thus, low values in the IC3 score at Hole 762C. Overall, the long-term variation in IC3 scores indicates changes in terrigenous (especially fluvial) input associated with climatic changes, namely, EECO and subsequent cooling.

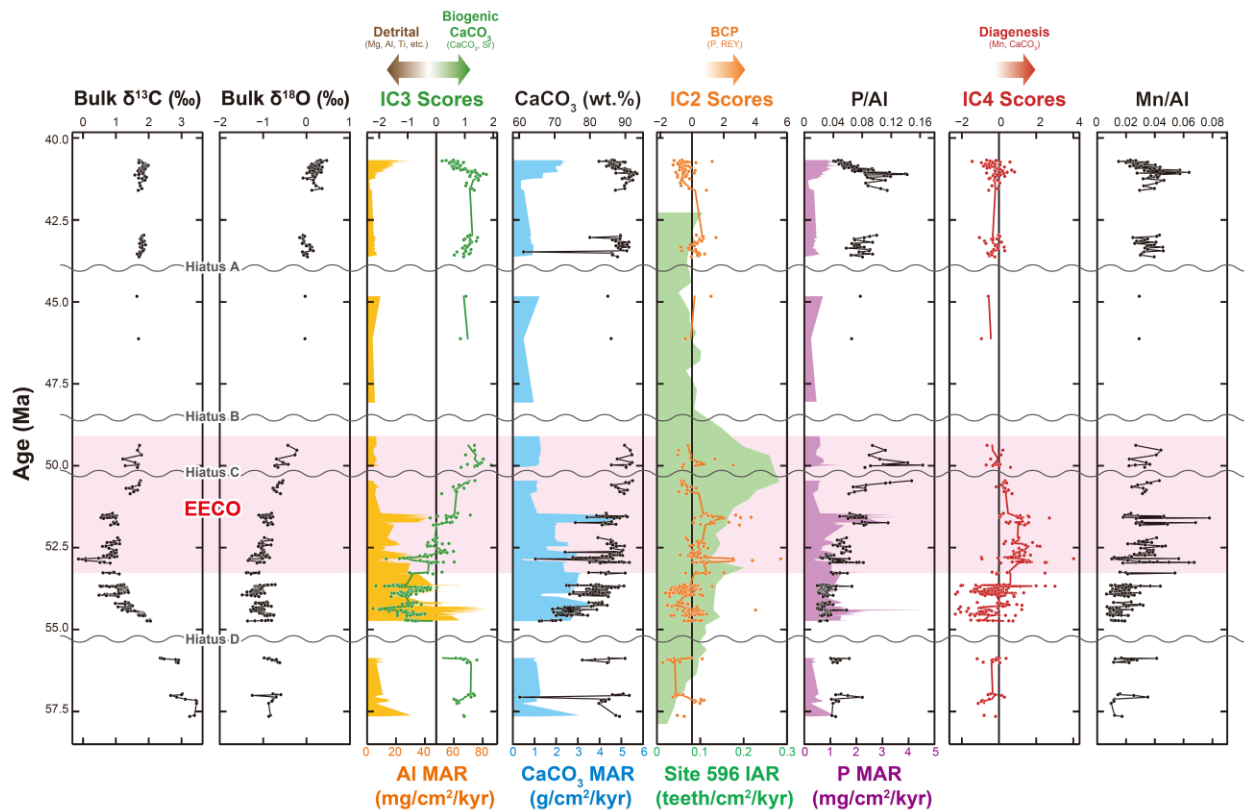


Figure 6. Secular variations of extracted IC scores of IC3, IC2, and IC4 from the bulk chemical composition. Bulk carbonate $\delta^{13}\text{C}$, $\delta^{18}\text{O}$, CaCO_3 abundances, P/Al, Mn/Al, and mass accumulation rates (MAR) of Al, CaCO_3 , P in Hole 762C are also shown. Ichthyolith accumulation rates (IAR) of the South Pacific pelagic realm (DSDP Site 596; Britten & Sibert, 2020) are also shown. The solid lines in IC3, IC2, and IC4 are the 5-point moving average. Grey wavy lines are hiatuses indicated by Shamrock et al. (2012). The MARs of CaCO_3 and Al were calculated using the sedimentation rate estimated in this study and dry bulk density based on a shipboard study (Haq et al. 1990).

5.3.2 Long-Term Biogenic Calcium Phosphate Abundances (IC2)

IC2 showed positive loadings of P, Y, and REE, except for Ce (Figure 4b). This element composition is typically observed in biogenic calcium phosphate (BCP), including the bones, teeth, and scales of marine vertebrates (Yasukawa et al., 2016, 2022). As BCP effectively adsorbs REE and Y, BCP in marine sediments is characterized by high REE enrichment (Kashiwabara et al., 2014; Takaya et al., 2018; Toyoda & Tokonami, 1990). Therefore, we considered that IC2 represents BCP in Hole 762C sediments.

As the long-term trend, the IC2 score showed positive values during 53–50 Ma, corresponding to the early stage of the EECO period (Figure 6). Further, the MAR of P also

elevated. These features indicate that high-level consumers (i.e., fish) in marine ecosystems prospered under the warm environment of the EECO at Hole 762C. The elevation of P/Al ratio at ~50 Ma may be due to the low input of terrigenous material rather than the increase of BCP flux because the MAR of P in this interval does not show any increase. The proliferation of fish during EECO has also been reported in the pelagic realm of the South Pacific Ocean, based on ichthyolith accumulation rates (DSDP Site 596; Britten & Sibert, 2020; Sibert et al., 2016; Figure 6). Our study indicates that the proliferation of marine vertebrates commonly occurs in relatively coastal regions in the Indian Ocean.

5.3.3 Long-Term Changes in the Diagenesis on Carbonate (IC4)

IC4 demonstrated positive loadings of Mn and CaCO₃, indicating that this IC reflects the coexistence of Mn and biogenic CaCO₃ (Figure 4d). Mn in carbonate sediments originates from two different processes during diagenesis: (1) Mn⁴⁺ precipitates as manganese oxide (MnO₂) with iron oxides under oxic conditions, and (2) Mn²⁺ is incorporated into the calcite lattice and/or precipitates as (Mn, Ca)CO₃ on the biogenic calcite shells under a relatively reducing environment (e.g., Barras et al., 2018; Boyle, 1983; Pingitore et al., 1988; Thomson et al., 1986). The strong positive correlation between Mn and CaCO₃, without a positive correlation to Fe in IC4 loading, suggests that this IC represents the latter process that occurred in the Hole 762C sediments.

Based on this interpretation, the positive values of the IC4 score during 53–50 Ma, and associated high Mn/Al suggest that the incorporation of Mn on biogenic CaCO₃ via diagenesis was enhanced during this period (Figure 6). As incorporation of Mn in biogenic calcite generally occurs under suboxic environments (Pingitore et al., 1988), the high IC4 value at Hole 762C may imply the occurrence of relatively reducing conditions in porewater and/or bottom water at the site during the early stage of EECO.

5.4 Geochemical Implication of Each IC on Hyperthermals

5.4.1 Change of CaCO₃ Contribution Associated with Hyperthermals (IC3)

On a shorter (~10⁵ yr) timescale, IC3 scores and CaCO₃ abundances exhibited several spike-like decreases, typically at the I1, J, and ETM3 horizons (Figure 7a). In addition, low IC3 scores (< 0) and a decrease in the MAR of CaCO₃ occurred at H2 and L events. These features indicate a decrease in the contribution of biogenic CaCO₃ at multiple hyperthermal horizons at Hole 762C. As it is well known that ocean acidification and shallowing of CCD occurred during hyperthermal events (e.g., Slotnick et al., 2015; Zachos et al., 2005, 2010), the decrease in IC3 scores associated with carbon isotope excursions (CIEs) at multiple hyperthermal horizons may reflect the repetitive shallowing of the CCD and the resulting decline in CaCO₃ flux at Hole 762C.

Additionally, an increase in detrital input may also contribute to a negative shift of the IC3 score during hyperthermals because the weathering of terrestrial material increased during the hyperthermals (e.g., Ravizza et al., 2001; Tanaka et al., 2022). The high MARs of Al during I1 and J events (40–70 mg/cm²/kyr) also suggest an increase in detrital input into the depositional area of Hole 762C during these two hyperthermals.

646 In contrast to the record at Hole 762C, a previous study that applied ICA to early
647 Eocene carbonate sediments from the southern Indian Ocean (ODP Site 752 and Hole 738C) did
648 not show clear excursions of IC scores reflecting biogenic CaCO_3 vs terrigenous content at H2,
649 I1, and ETM3, despite the paleo-depth of both sites being close to that of Hole 762C (~1000–
650 1300 m; Yasukawa et al., 2017). Therefore, the magnitude of the reduction in carbonate rain
651 flux due to CCD shallowing or the increase in detrital materials during hyperthermals could
652 have been regionally variable.

653 The H2 horizon at Hole 762C did not exhibit a clear negative excursion of IC3 scores
654 and CaCO_3 abundances (Figure 6b; Supporting Figure S11b). The relatively minor variation at
655 the H2 horizon compared to that at the I1, J, and ETM3 horizons indicates that the magnitude of
656 CCD shallowing and the reduction of carbonate rain flux during the H2 event were smaller than
657 those during other events. This feature is consistent with the Atlantic record (Walvis Ridge;
658 Stap et al., 2009, 2010) and suggests that the magnitude of CCD shallowing could have been
659 variable between each hyperthermal event (Leon-Rodriguez & Dickens, 2010).

660 At the Paleocene-Eocene boundary of Hole 762C, the PETM horizon is incomplete
661 because of a hiatus that ranges ~1 Myr (Hiatus D; Shamrock et al., 2012). The gap of the
662 nannofossil assemblage across this hiatus without an obvious clay-rich layer suggests that the
663 hiatus might be caused not by a chemical erosion (i.e., carbonate dissolution) but by a physical
664 erosion (Supporting Figure S7). Considering that an incomplete record of the PETM is also
665 reported from a lower latitude, well above the CCD (paleodepth ~1,500 m) site in the Indian
666 Ocean (IODP Hole 1443A; Barnet et al., 2020), the occurrence of such a hiatus might be not on
667 a local scale but on a regional scale. Although we cannot constrain the causal factors at this
668 stage, the changes in the ocean circulation pattern during PETM (e.g., Abbott et al., 2016; Bice
669 & Marotzke, 2002) could have contributed to the emplacement of hiatuses observed in the low-
670 to mid-latitude Indian Ocean.

671

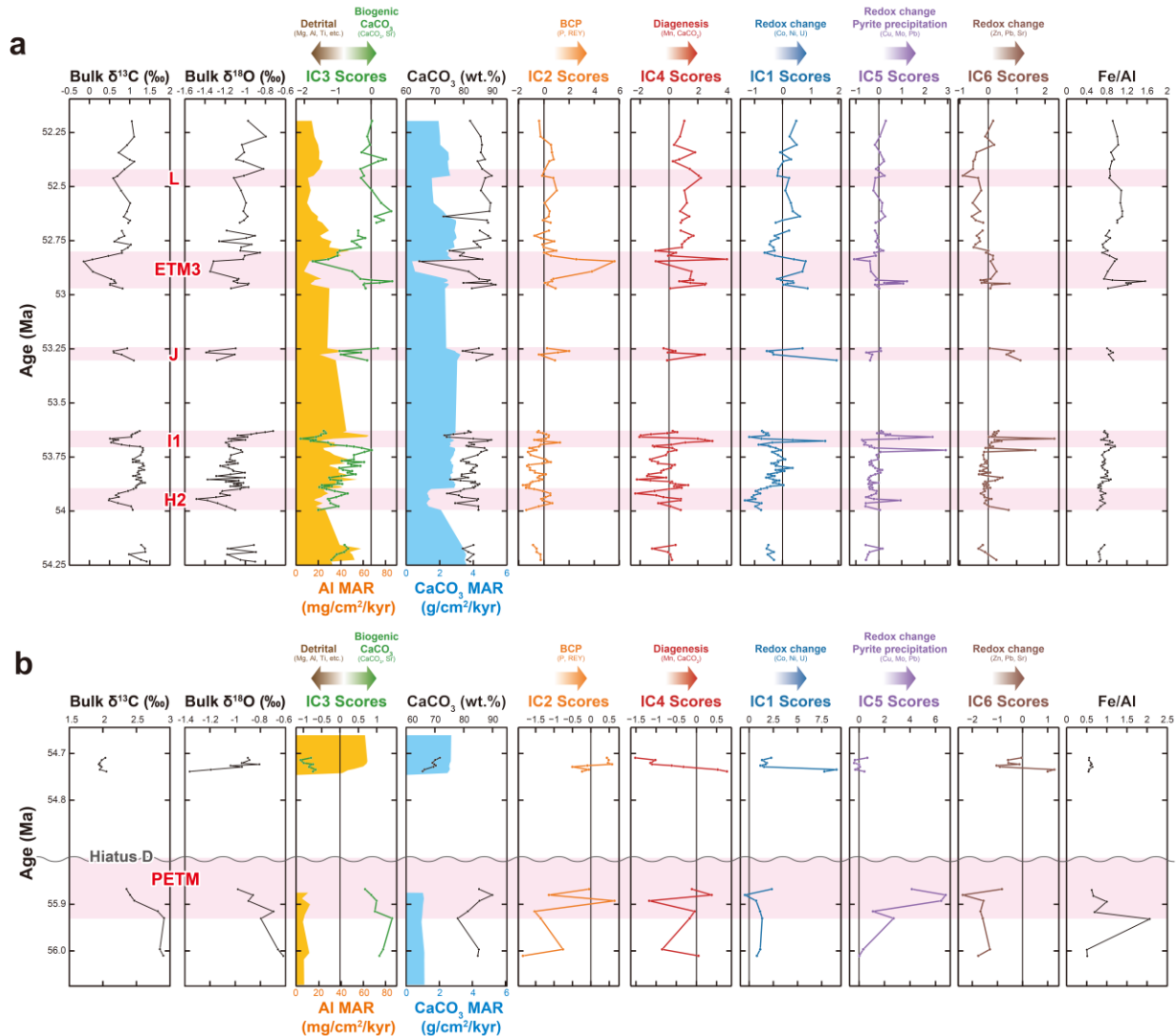


Figure 7. Variations of extracted IC scores from the bulk chemical composition of interval of (a) H2 – L event and (b) onset of PETM. Bulk carbonate $\delta^{13}\text{C}$, $\delta^{18}\text{O}$, CaCO_3 abundances, Fe/Al ratio, and mass accumulation rates (MAR) of Al, CaCO_3 of Hole 762C are also shown. Hiatus D is shown by a grey waved line (based on Shamrock et al., 2012).

5.4.2 Biogenic Calcium Phosphate Contribution Associated with Hyperthermals (IC2)

In the sediments of Hole 762C, the IC2 score repetitively showed spike-like increases at the PETM (onset; 55.93 Ma), H2, I1, J, and ETM3 horizons (Figure 7). As IC2 primarily reflects the contribution of BCP, the systematic increase in IC2 scores at hyperthermal horizons indicates an increase in the contribution of BCP associated with the warming events. Therefore,

the proliferation of fish at Hole 762C may be linked to both the long-term warming trend and the short-lived hyperthermals.

Arguments persist regarding the enhancement of biological productivity during hyperthermals (e.g., Bains et al., 2000; Bralower, 2002; Gibbs et al., 2006; Ma et al., 2014; Winguth et al., 2012; Yasukawa et al., 2017; Zhou et al., 2014). The increase in nutrient input due to an increased weathering flux under the warm hyperthermal climate may have triggered the proliferation of marine vertebrates at Hole 762C. However, Sites 752 and 738 showed no clear signature of BCP increase at H2, I1, or ETM3 (Yasukawa et al., 2017). The distinct increase in BCP observed at Hole 762C may be attributed to its proximity to continents, which results in a relatively higher availability of nutrients compared with that in the pelagic area. Our results indicate that the prosperity of marine vertebrates may have sensitively responded to hyperthermals with significant regional variation, even within the Indian Ocean.

5.4.3 Post-Depositional Geochemical Processes Associated with Hyperthermals (IC1, IC4, IC5, and IC6)

As previously described, IC4 was interpreted as the diagenetic signature on carbonate characterized by the positive correlation between Mn and CaCO_3 . The depletion and reconcentration of Mn have been interpreted as diagenetic signatures associated with reduction and oxidation in the sediments (e.g., Burdige & Gieskes, 1983); thus, the fluctuations of IC4 score at hyperthermal horizons can be interpreted as changes in the sediment redox condition.

Additionally, the IC1, IC5, and IC6 are interpreted as the redox-related behavior of metal elements, including Co, Ni, U, Cu, Mo, Pb, Zn, and Sr (Figure 4a, e, f; Supporting Text S4, Figure S12). As of their easiness in remobilization associated with the redox condition, the variation in these elements' concentration and, thus, IC scores reflect the changes in the redox condition of sediment pore water and/or bottom seawater (e.g., Calvert & Pederson, 1993; Thomson et al., 1993). However, IC1, IC5, and IC6 exhibited variations that differed from IC4 as they did not show a clear correlation with CaCO_3 (Figure 4).

Various geochemical processes have been proposed to explain the concentration or depletion of redox-sensitive metals in marine sediments, including remobilization and precipitation of metals due to the change in valence corresponding to the redox state of sediment pore water (e.g., Calvert & Pederson, 1993) and co-precipitation with authigenic pyrite (Algeo & Maynard, 2004; Huerta-Diez & Morse, 1992). Such differences in concentration or depletion processes may cause separation between IC1, IC5, and IC6. In particular, a positive value of IC5 score at the beginning of ETM3 appears to correspond to the Fe/Al peak (Figure 7a), indicating the relationship between the occurrence of authigenic pyrite and co-precipitation of Cu, Mo, and Pb indicated by IC5 scores.

IC1, IC5, and IC6 exhibited sharp peaks near hyperthermal horizons, and peaks tend to shift slightly between each IC (Figure 7a). At the horizon of the PETM-onset, there was a positive excursion of IC5 at the onset of CIE and peaks of IC1 and IC6 above the Hiatus D (Figure 7b). Therefore, we suggest that these ICs capture the enrichment and dissolution of redox-sensitive elements in the PETM layer of Hole 762C. At the horizon of the I1 event, IC1 peaks near the CIE level, and IC5 and IC6 peak above and below the CIE (Figure 7a). Such

obvious excursions of IC score peaks occurring nearby hyperthermals are also observed in the H2, J, and ETM3 horizons, suggesting the occurrence of elemental enrichment and dissolution systematically occurred at the hyperthermal events. However, there may be variations in the magnitude of redox change in each event.

The reductive horizons in Hole 762C identified through ICA may indicate that the redox state of the porewater and bottom water at the Exmouth Plateau in the eastern Indian Ocean fluctuated during hyperthermals. Regarding the PETM, previous studies have reported that the enrichment and dissolution of redox-sensitive elements indicate that the redox state of the bottom water became reductive (~suboxic) at several sites in the Atlantic and Indian Oceans (Chun et al., 2010; Pälike et al., 2014). Our results are consistent with these previous studies, suggesting that porewater or bottom-water redox changes occurred in the mid-latitude eastern Indian Ocean. Furthermore, our data indicate novel insights into repetitive redox changes associated with the modest, multiple hyperthermals after the PETM. In addition, Zhou et al. (2014) suggested the occurrence of upper ocean deoxygenation during the PETM based on the I/Ca record of bulk carbonate sediments from each ocean basin, including Hole 762C. Therefore, the redox condition in hyperthermal horizons of Hole 762C sediments is potentially linked to the upper ocean dissolved oxygen concentration and primary production rate at the photic zone.

5.5 Insights into Decoding the Paleoenvironmental Changes in Hyperthermals with ICA

Our study sheds light on the complex interplay between transient global warmings (i.e., hyperthermals) and paleoceanographic responses. As we noted in Section 4.3., the ICs extracted from the bulk chemical composition were statistically independent. In other words, each IC reflected a signature imprinted in sediments that can be considered a distinct geochemical feature. In reconstructing the paleoceanographic record at Hole 762C, each IC reflects a distinct aspect of paleoenvironmental changes during hyperthermals. Under the warm hyperthermal climate, increased chemical weathering and riverine drainage could have occurred (e.g., Dickson et al., 2015; Pogge von Strandmann et al., 2021; Ravizza et al., 2001; Tanaka et al., 2022). The increase in the relative contribution of the fluvial detrital component, represented by negative excursions in IC3, can be interpreted as a result of these environmental changes. Additionally, increased continental runoff may have also caused a significant input of nutrients to the continental margin. Given that Hole 762C is located on the northwestern margin of offshore Australia, this increase in nutrient supply could have enhanced the marine primary productivity around the site. The positive excursions of IC2, which indicate an increase of BCP accumulation at hyperthermal horizons, suggest another vestige of the warming events from a biological/ecological perspective.

The results of ICA also indicate the impact of hyperthermals on seawater chemistry. During hyperthermals, at least locally/regionally, oceans are thought to have stratified due to warming (e.g., Sluijs et al., 2009; Tripathi & Elderfield, 2005; Willard et al., 2019; Zachos et al., 2003). Furthermore, although regional variations may have existed, bottom seawater is considered to have become hypoxic–suboxic (e.g., Kaiho et al., 2006; Pälike et al., 2014; Papadomanolaki et al., 2022; Zhou et al., 2016). Excessive sedimentation of organic matter due to the increased nutrient supply from land and high productivity in the surface ocean may have induced bottom-water hypoxia on the continental shelf owing to enhanced oxygen consumption (Sluijs et al., 2014), as well as decreased dissolved oxygen due to high water temperatures

associated with hyperthermals. Such environmental changes during hyperthermals could have resulted in changes in the redox state at the sediment-water interface and the uppermost sediment. This process could have mobilized several redox-sensitive elements after deposition and caused the pyrite precipitation in the reductive zone. Depending on the differences in the kinetics and chemical affinity of each element, redistribution, and enrichment of different sets of elements might have occurred in the sediment. These distinct features were subsequently separated as IC1, IC4, IC5, and IC6, which are mutually superimposed as statistically independent data structures in the sediment. Overall, the result of ICA on the bulk chemical composition of Hole 762C sediments provides insights into various paleoceanographic processes during hyperthermals; each independent signature of multi-elemental geochemistry reflects different aspects of the effects of global warming on terrestrial and marine environments.

As our study is based on the bulk chemical composition, our discussion remains limited to suggesting the geological phenomena that result in the accumulation and migration of source materials at this site. To further validate these interpretations, future investigations using proxies for continental chemical weathering (e.g., $^{187}\text{Os}/^{188}\text{Os}$ and $\delta^7\text{Li}$; Pogge von Strandmann et al., 2021; Ravizza et al., 2001; Tanaka et al., 2022), biological productivity (e.g., barite accumulation rate and $\delta^{138/134}\text{Ba}$; Bains et al., 2000; Bridgestock et al., 2019; Ma et al., 2014; Miyazaki et al., 2023), paleo-seawater pH (e.g., $\delta^{11}\text{B}$; Anagnostou et al., 2020; Gutjahr et al., 2017; Harper et al., 2020; Henehan et al., 2020), and paleo-redox conditions (e.g., $\delta^{98/95}\text{Mo}$ and $\delta^{15}\text{N}$; Auderset et al., 2022; Dickson, 2017; Siebert et al., 2003) may be necessary. By combining the results of ICA applied to bulk chemistry with a multi-proxy record involving various isotopes, we expect to gain a deeper understanding of the Earth system's responses to transient global warmings during the early Paleogene.

6 Conclusions

We newly reported $\delta^{13}\text{C}$, $\delta^{18}\text{O}$, and the chemical composition of bulk carbonate sediments at ODP Hole 762C on the Exmouth Plateau in the eastern Indian Ocean and identified the long-term climatic trend (i.e., the EECO followed by the cooling) and six transient hyperthermals (i.e., PETM (onset), H2, I1, J, ETM3, and L). Through the independent component analysis (ICA) on the bulk chemical compositions, we extracted six ICs, including the mixing relation between biogenic CaCO_3 and detrital material (IC3), biogenic calcium phosphate (IC2), diagenetic processes involving Mn-carbonate (IC4), and post-depositional remobilization of redox-sensitive elements (IC1, IC5, IC6) associated with diagenesis and changes in redox conditions. As a result of ICA, a decrease in the contribution of biogenic CaCO_3 or an increase in the riverine terrigenous input relating to significant oceanographic and terrestrial environmental changes in the Early Eocene (~54.5–51.8 Ma), suggested by the low IC3 score. In addition, the proliferation of marine vertebrates and the occurrence of reducing sedimentary environments during the early stage of EECO are suggested by IC2 and IC4, respectively. During hyperthermals, negative excursions in IC3 scores were repetitively observed, indicating CCD shallowing or an increase of detrital input due to enhanced continental weathering during these transient warming events. Also, the proliferation of marine vertebrates at hyperthermals is implied by IC2. Other ICs (IC1, IC4, IC5, and IC6) representing the behaviors of redox-sensitive elements, show peaks around the hyperthermals. This feature suggests that changes in the redox state of porewater or bottom

water occurred associated with hyperthermals at Hole 762C. Our study sheds light on the behaviors of biological and oceanographic responses of mid-latitude eastern Indian Ocean on early Paleogene climate changes. Further research using multiple isotopic analyses (e.g., $^{187}\text{Os}/^{188}\text{Os}$, $\delta^{138}\text{Ba}$, and $\delta^7\text{Li}$), microscopic analysis on biogenic, terrigenous, and authigenic materials, and higher-resolution time-series analysis will provide a more detailed understanding of the Paleogene Warmhouse/Hothouse climates in the Indian Ocean.

Acknowledgments

This research was funded by the Japan Society for Promotion of Science (JSPS) KAKENHI Grants No. 20H05658 to Y. Kato, No. 17H01361 to K.N., No. 20H02678 to K.Y., and No. 20J22396 and 23K19025 to Y. Kuwahara. This study was performed under the cooperative research program of Center for Advanced Marine Core Research (present Marine Core Research Institute), Kochi University Accept No. 21A019 and 21B018 to Y. Kuwahara. This research used samples provided by the International Ocean Discovery Program (IODP). We appreciate Y. Kubo, IODP Curator at Kochi Core Center, for his invaluable support in sampling. We appreciate the support of Y. Itabashi, The University of Tokyo, with bulk chemical analyses. We are grateful to N. Fujimura and N. Shibuya at Kochi University, for their analytical support in stable isotope analyses. We thank three anonymous reviewers for thoughtful and constructive comments, and M. Huber for editorial handling.

Open Research

The stable isotope records and bulk chemical composition data are also available on Kuwahara et al. (2024b). The R script for implementing ICA (fastICA algorithm) used in this study is available on Kuwahara et al. (2024a). This code was modified from an R script previously published by Yasukawa et al. (2023).

References

- Abbott, A. N., Haley, B. A., Tripathi, A. K., & Frank, M. (2016), Constraints on ocean circulation at the Paleocene-Eocene Thermal Maximum from neodymium isotopes. *Climate of the Past*, 12(4), 837–847. <https://doi.org/10.5194/cp-12-837-2016>
- Algeo, T. J., & Maynard, J. B. (2004), Trace-element behavior and redox facies in core shales of Upper Pennsylvanian Kansas-type cyclothems. *Chemical Geology*, 206(3–4), 289–318. <https://doi.org/10.1016/j.chemgeo.2003.12.009>
- Alibo, D. S., & Nozaki, Y. (1999), Rare earth elements in seawater: Particle association, shale-normalization, and Ce oxidation. *Geochimica et Cosmochimica Acta*, 63(3–4). [https://doi.org/10.1016/S0016-7037\(98\)00279-8](https://doi.org/10.1016/S0016-7037(98)00279-8)
- Anagnostou, E., John, E. H., Babila, T. L., Sexton, P. F., Ridgwell, A., & Lunt, D. J. (2020), Proxy evidence for state-dependence of climate sensitivity in the Eocene greenhouse. *Nature Communications*, 11(1), 4436. <https://doi.org/10.1038/s41467-020-17887-x>
- Anagnostou, E., John, E. H., Edgar, K. M., Foster, G. L., Ridgwell, A., Inglis, G. N., Pancost, R. D., Lunt, D. J., & Pearson, P. N. (2016), Changing atmospheric CO₂ concentration was the primary driver of early Cenozoic climate. *Nature*, 533(7603), 380–384. <https://doi.org/10.1038/nature17423>
- Assonov, S., Groening, M., Fajgelj, A., Hélie, J. F., & Hillaire-Marcel, C. (2020). Preparation and characterisation of IAEA-603, a new primary reference material aimed at the VPDB scale realisation for $\delta^{13}\text{C}$ and $\delta^{18}\text{O}$ determination. *Rapid Communications in Mass Spectrometry*, 34(20). <https://doi.org/10.1002/rcm.8867>

- Auderset, A., Moretti, S., Taphorn, B., Ebner, P.-R., Kast, E., Wang, X. T., Schiebel, R., Sigman, D. M., Haug, G. H., & Martínez-García, A. (2022), Enhanced ocean oxygenation during Cenozoic warm periods. *Nature*, 609(7925), 77–82. <https://doi.org/10.1038/s41586-022-05017-0>
- Bains, S., Norris, R. D., Corfield, R. M., & Faul, K. L. (2000), Termination of global warmth at the Palaeocene/Eocene boundary through productivity feedback. *Nature*, 407(6801), 171–174. <https://doi.org/10.1038/35025035>
- Barnet, J. S. K., Harper, D. T., LeVay, L. J., Edgar, K. M., Henehan, M. J., Babila, T. L., Ullmann, C. V., Leng, M. J., Kroon, D., Zachos, J. C., & Littler, K. (2020), Coupled evolution of temperature and carbonate chemistry during the Paleocene–Eocene; new trace element records from the low latitude Indian Ocean. *Earth and Planetary Science Letters*, 545, 116414. <https://doi.org/10.1016/j.epsl.2020.116414>
- Barnet, J. S. K., Littler, K., Westerhold, T., Kroon, D., Leng, M. J., Bailey, I., Röhl, U., & Zachos, J. C. (2019), A High-Fidelity Benthic Stable Isotope Record of Late Cretaceous–Early Eocene Climate Change and Carbon-Cycling. *Paleoceanography and Paleoclimatology*, 34(4), 672–691. <https://doi.org/10.1029/2019PA003556>
- Barras, C., Mouret, A., Nardelli, M. P., Metzger, E., Petersen, J., La, C., Filipsson, H. L., & Jorissen, F. (2018), Experimental calibration of manganese incorporation in foraminiferal calcite. *Geochimica et Cosmochimica Acta*, 237, 49–64. <https://doi.org/10.1016/j.gca.2018.06.009>
- Berndt, C., Planke, S., Alvarez Zarikian, C. A., Frieling, J., Jones, M. T., Millett, J. M., Brinkhuis, H., Bünz, S., Svensen, H. H., Longman, J., Scherer, R. P. et al. (2023), Shallow-water hydrothermal venting linked to the Palaeocene–Eocene Thermal Maximum. *Nature Geoscience*, 16(9), 803–809. <https://doi.org/10.1038/s41561-023-01246-8>
- Bice, K. L., & Marotzke, J. (2002), Could changing ocean circulation have destabilized methane hydrate at the Paleocene/Eocene boundary? *Paleoceanography*, 17(2), 8–1–8–12. <https://doi.org/10.1029/2001pa000678>
- Bilal, A., & McClay, K. (2022), Tectonic and stratigraphic evolution of the central Exmouth Plateau, NW Shelf of Australia. *Marine and Petroleum Geology*, 136, 105447. <https://doi.org/10.1016/j.marpetgeo.2021.105447>
- Bohaty, S. M., & Zachos, J. C. (2003), Significant Southern Ocean warming event in the late middle Eocene. *Geology*, 31(11), 1017–1020. <https://doi.org/10.1130/g19800.1>
- Boyle, E. A. (1983), Manganese carbonate overgrowths on foraminifera tests. *Geochimica et Cosmochimica Acta*, 47(10), 1815–1819. [https://doi.org/10.1016/0016-7037\(83\)90029-7](https://doi.org/10.1016/0016-7037(83)90029-7)
- Bralower, T. J. (2002), Evidence of surface water oligotrophy during the Paleocene-Eocene thermal maximum: Nannofossil assemblage data from Ocean Drilling Program Site 690, Maud Rise, Weddell Sea. *Paleoceanography*, 17(2), 1023. <https://doi.org/10.1029/2001pa000662>
- Bridgestock, L., Hsieh, Y., Porcelli, D., & Henderson, G. M. (2019), Increased export production during recovery from the Paleocene–Eocene thermal maximum constrained by sedimentary Ba isotopes. *Earth and Planetary Science Letters*, 510, 53–63. <https://doi.org/10.1016/j.epsl.2018.12.036>
- Britten, G. L., & Sibert, E. C. (2020), Enhanced fish production during a period of extreme global warmth. *Nature Communications*, 11(1), 5636. <https://doi.org/10.1038/s41467-020-19462-w>
- Burdige, D. J., & Gieskes, J. M. (1983), A pore water/solid phase diagenetic model for manganese in marine sediments. *American Journal of Science*, 283(1), 29–47. <https://doi.org/10.2475/ajs.283.1.29>
- Burton, Z. F. M., McHargue, T., Kremer, C. H., Bloch, R. B., Gooley, J. T., Jaikla, C., Harrington, J., & Graham, S. A. (2023), Peak Cenozoic warmth enabled deep-sea sand deposition. *Scientific Reports*, 13(1), 1276. <https://doi.org/10.1038/s41598-022-27138-2>
- Calvert, S. E., & Pedersen, T. F. (1993), Geochemistry of Recent oxic and anoxic marine sediments: Implications for the geological record. *Marine Geology*, 113(1–2), 67–88. [https://doi.org/10.1016/0025-3227\(93\)90150-T](https://doi.org/10.1016/0025-3227(93)90150-T)
- Charisi, S. D., & Schmitz, B. (1996), Early Eocene palaeoceanography and palaeoclimatology of the eastern North Atlantic: stable isotope results for DSDP Hole 550. *Geological Society, London, Special Publications*, 101(1), 457–472. <https://doi.org/10.1144/GSL.SP.1996.101.01.22>
- Chun, C. O. J., Delaney, M. L., & Zachos, J. C. (2010), Paleoredox changes across the Paleocene-Eocene thermal maximum, Walvis Ridge (ODP Sites 1262, 1263, and 1266): Evidence from Mn and U enrichment factors. *Paleoceanography*, 25(4), 1–13. <https://doi.org/10.1029/2009PA001861>
- Clarkson, M. O., Lenton, T. M., Andersen, M. B., Bagard, M. L., Dickson, A. J., & Vance, D. (2021), Upper limits on the extent of seafloor anoxia during the PETM from uranium isotopes. *Nature Communications*, 12(1), 399. <https://doi.org/10.1038/s41467-020-20486-5>
- Cramer, B. S., Wright, J. D., Kent, D. V., & Aubry, M. P. (2003), Orbital climate forcing of $\delta^{13}\text{C}$ excursions in the late Paleocene-early Eocene (chrons C24n-C25n). *Paleoceanography*, 18(4), 1097. <https://doi.org/10.1029/2003PA000909>

- Dallanave, E., Agnini, C., Bachtadse, V., Muttoni, G., Crampton, J. S., Percy Strong, C., Hines, B. R., Hollis, C. J., & Slotnick, B. S. (2015), Early to middle Eocene magneto-biochronology of the southwest Pacific Ocean and climate influence on sedimentation: Insights from the Mead Stream section, New Zealand. *Bulletin of the Geological Society of America*, 127(5–6), 643–660. <https://doi.org/10.1130/B31147.1>
- D’haenens, S., Bornemann, A., Claeys, P., Röhl, U., Steurbaut, E., & Speijer, R. P. (2014), A transient deep-sea circulation switch during Eocene Thermal Maximum 2. *Paleoceanography*, 29(5), 370–388. <https://doi.org/10.1002/2013PA002567>
- Dickens, G. R., Neil, J. R. O., Rea, D. K., & Owen, R. M. (1995), Dissociation of oceanic methane hydrate as a cause of the carbon isotope excursion at the end of the Paleocene. *Paleoceanography*, 10(6), 965–971. <https://doi.org/10.1029/95PA02087>
- Dickson, A. J. (2017), A molybdenum-isotope perspective on Phanerozoic deoxygenation events. *Nature Geoscience*, 10(10), 721–726. <https://doi.org/10.1038/NGEO3028>
- Dickson, A. J., Cohen, A. S., Coe, A. L., Davies, M., Shcherbinina, E. A., & Gavrillov, Y. O. (2015), Evidence for weathering and volcanism during the PETM from Arctic Ocean and Peri-Tethys osmium isotope records. *Palaeogeography, Palaeoclimatology, Palaeoecology*, 438, 300–307. <https://doi.org/10.1016/j.palaeo.2015.08.019>
- Dunlea, A. G., Murray, R. W., Sauvage, J., Spivack, A. J., Harris, R. N., & D’Hondt, S. (2015), Dust, volcanic ash, and the evolution of the South Pacific Gyre through the Cenozoic. *Paleoceanography*, 30(8), 1078–1099. <https://doi.org/10.1002/2015PA002829>
- Dutton, A., Lohmann, K. C., & Leckie, R. M. (2005), Insights from the Paleogene tropical Pacific: Foraminiferal stable isotope and elemental results from Site 1209, Shatsky Rise. *Paleoceanography*, 20(3), PA3004. <https://doi.org/10.1029/2004PA001098>
- Galbrun, B. (1992), Magnetostratigraphy of Upper Cretaceous and Lower Tertiary sediments, Sites 761 and 762, Exmouth Plateau, northwest Australia. *Proc. Scientific Results, ODP, Leg 122, Exmouth Plateau*, 122, 699–716. <https://doi.org/10.2973/odp.proc.sr.122.149.1992>
- Gibbs, S. J., Bralower, T. J., Bown, P. R., Zachos, J. C., & Bybell, L. M. (2006), Shelf and open-ocean calcareous phytoplankton assemblages across the Paleocene-Eocene thermal maximum: Implications for global productivity gradients. *Geology*, 34(4), 233–236. <https://doi.org/10.1130/G22381.1>
- Gutjahr, M., Ridgwell, A., Sexton, P. F., Anagnostou, E., Pearson, P. N., Pälike, H., Norris, R. D., Thomas, E., & Foster, G. L. (2017), Very large release of mostly volcanic carbon during the Palaeocene-Eocene Thermal Maximum. *Nature*, 548(7669), 573–577. <https://doi.org/10.1038/nature2364>
- Guttman, L. (1954), Some necessary conditions for common factor analysis. *Psychometrika*, 19, 149–161. <https://doi.org/10.1007/BF02289162>
- Haq, B. U., Boyd, R. L., Exon, N. F., & Von Rad, U. (1992), Evolution of the central Exmouth Plateau: a post-drilling perspective. In *Proceedings of the Ocean Drilling Program, Scientific Results* (Vol. 122, pp. 801–816). College Station, TX: Ocean Drilling Program. <https://doi.org/10.2973/odp.proc.sr.122.182.1992>
- Haq, B. U., von Rad, U. & O’Connell, S. (1990), Site 762. In Haq, B. U., von Rad, U. & O’Connell, S. *Proceedings of the ocean drilling program, Initial Reports, Leg 122*, (Vol. 122, pp. 213–288). College Station, TX: Ocean Drilling Program. <https://doi.org/10.2973/odp.proc.ir.122.108.1990>
- Harper, D. T., Hönisch, B., Zeebe, R. E., Shaffer, G., Haynes, L. L., Thomas, E., & Zachos, J. C. (2020), The Magnitude of Surface Ocean Acidification and Carbon Release During Eocene Thermal Maximum 2 (ETM-2) and the Paleocene-Eocene Thermal Maximum (PETM). *Paleoceanography and Paleoclimatology*, 35(2), e2019PA003699. <https://doi.org/10.1029/2019PA003699>
- Henehan, M. J., Edgar, K. M., Foster, G. L., Penman, D. E., Hull, P. M., Greenop, R., Anagnostou, E., & Pearson, P. N. (2020), Revisiting the Middle Eocene Climatic Optimum “Carbon Cycle Conundrum” With New Estimates of Atmospheric pCO₂ From Boron Isotopes. *Paleoceanography and Paleoclimatology*, 35(6), e2019PA003713. <https://doi.org/10.1029/2019PA003713>
- Hodell, D. A., Kamenov, G. D., Hathorne, E. C., Zachos, J. C., Röhl, U., & Westerhold, T. (2007), Variations in the strontium isotope composition of seawater during the Paleocene and early Eocene from ODP Leg 208 (Walvis Ridge). *Geochemistry, Geophysics, Geosystems*, 8(9), Q09001. <https://doi.org/10.1029/2007GC001607>
- Hollis, C. J., Hines, B. R., Littler, K., Villasante-Marcos, V., Kulhanek, D. K., Strong, C. P., Zachos, J. C., Eggins, S. M., Northcote, L., & Phillips, A. (2015), The Paleocene-Eocene Thermal Maximum at DSDP Site 277, Campbell Plateau, southern Pacific Ocean. *Climate of the Past*, 11(7), 1009–1025. <https://doi.org/10.5194/cp-11-1009-2015>
- Huerta-Diaz, M. A., & Morse, J. W. (1992), Pyritization of trace metals in anoxic marine sediments. *Geochimica et Cosmochimica Acta*, 56(7), 2681–2702. [https://doi.org/10.1016/0016-7037\(92\)90353-K](https://doi.org/10.1016/0016-7037(92)90353-K)

- Hyland, E. G., & Sheldon, N. D. (2013), Coupled CO₂-climate response during the Early Eocene Climatic Optimum. *Palaeogeography, Palaeoclimatology, Palaeoecology*, 369, 125–135. <https://doi.org/10.1016/j.palaeo.2012.10.011>
- Hyland, E. G., Sheldon, N. D., & Cotton, J. M. (2017), Constraining the early Eocene climatic optimum: A terrestrial interhemispheric comparison. *Bulletin of the Geological Society of America*, 129(1–2), 244–252. <https://doi.org/10.1130/B31493.1>
- Imai, N., Terashima, S., Itoh, S., & Ando, A. (1995), 1994 Compilation of analytical data for minor and trace elements in seventeen GSJ geochemical reference samples, “Igneous rock series.” *Geostandards and Geoanalytical Research*, 19(2), 135–213. <https://doi.org/10.1111/j.1751-908X.1995.tb00158.x>
- Ishizuka, O., Tani, K., Reagan, M. K., Kanayama, K., Umino, S., Harigane, Y., Sakamoto, I., Miyajima, Y., Yuasa, M., & Dunkley, D. J. (2011), The timescales of subduction initiation and subsequent evolution of an oceanic island arc. *Earth and Planetary Science Letters*, 306(3–4), 229–240. <https://doi.org/10.1016/j.epsl.2011.04.006>
- Iwamori, H., & Albarède, F. (2008), Decoupled isotopic record of ridge and subduction zone processes in oceanic basalts by independent component analysis. *Geochemistry, Geophysics, Geosystems*, 9(4), Q04033. <https://doi.org/10.1029/2007GC001753>
- Jones, R. W., & Wonders, A. A. H. (1992), Benthic foraminifers and paleobathymetry of Barrow Group (Berriasian–Valanginian) deltaic sequences, Sites 762 and 763, Northwest Shelf, Australia. *Proc. Scientific Results, ODP, Leg 122, Exmouth Plateau*, 122, 557–568. <https://doi.org/10.2973/odp.proc.sr.122.174.1992>
- Kaiho, K., Takeda, K., Petrizzo, M. R., & Zachos, J. C. (2006), Anomalous shifts in tropical Pacific planktonic and benthic foraminiferal test size during the Paleocene-Eocene thermal maximum. *Palaeogeography, Palaeoclimatology, Palaeoecology*, 237(2–4), 456–464. <https://doi.org/10.1016/j.palaeo.2005.12.017>
- Kaiser, H. F. (1960), The application of electronic computers to factor analysis. *Educational and Psychological Measurement*, 20, 141–151. <https://doi.org/10.1177/001316446002000116>
- Kashiwabara, T., Toda, R., Fujinaga, K., Honma, T., Takahashi, Y., & Kato, Y. (2014), Determination of host phase of lanthanum in deep-sea REY-rich mud by XAFS and μ -XRF using high-energy synchrotron radiation. *Chemistry Letters*, 43(2), 199–200. <https://doi.org/10.1246/cl.130853>
- Kato, Y., Fujinaga, K., Nakamura, K., Takaya, Y., Kitamura, K., Ohta, J., Toda, R., Nakashima, T., & Iwamori, H. (2011), Deep-sea mud in the Pacific Ocean as a potential resource for rare-earth elements. *Nature Geoscience*, 4(8), 535–539. <https://doi.org/10.1038/ngeo1185>
- Kato, Y., Fujinaga, K., & Suzuki, K. (2005), Major and trace element geochemistry and Os isotopic composition of metalliferous umbers from the Late Cretaceous Japanese accretionary complex. *Geochemistry, Geophysics, Geosystems*, 6(7), Q07004. <https://doi.org/10.1029/2005GC000920>
- Kennett, P., & Stott, D. (1991), Abrupt deep-sea warming, palaeoceanographic changes and benthic extinctions at the end of the Palaeocene. *Nature*, 353, 225–229.
- Kirtland Turner, S., Sexton, P. F., Charles, C. D., & Norris, R. D. (2014), Persistence of carbon release events through the peak of early Eocene global warmth. *Nature Geoscience*, 7(10), 748–751. <https://doi.org/10.1038/NCEO2240>
- Komar, N., Zeebe, R. E., & Dickens, G. R. (2013), Understanding long-term carbon cycle trends: The late Paleocene through the early Eocene. *Paleoceanography*, 28(4), 650–662. <https://doi.org/10.1002/palo.20060>
- Kuwahara, Y., Yasukawa, K., Tanaka, E., Nakamura, K., Ikehara, M., & Kato, Y. (2024a), R scripts for independent component analysis on bulk chemical composition dataset of ODP Hole 762C sediments from mid-latitude Indian Ocean (ICA). [Software] *Zenodo*. <https://doi.org/10.5281/zenodo.12571435>
- Kuwahara, Y., Yasukawa, K., Tanaka, E., Nakamura, K., Ikehara, M., & Kato, Y. (2024b), Stable isotope records and bulk chemical compositions of the early Paleogene intervals of ODP Hole 762C [Data set]. *Zenodo*. <https://doi.org/10.5281/zenodo.13731575>
- Lauretano, V., Littler, K., Polling, M., Zachos, J. C., & Lourens, L. J. (2015), Frequency, magnitude and character of hyperthermal events at the onset of the Early Eocene Climatic Optimum. *Climate of the Past*, 11(10), 1313–1324. <https://doi.org/10.5194/cp-11-1313-2015>
- Le Houedec, S., Meynadier, L., & Allègre, C. J. (2012), Nd isotope systematics on ODP Sites 756 and 762 sediments reveal major volcanic, oceanic and climatic changes in South Indian Ocean over the last 35Ma. *Earth and Planetary Science Letters*, 327–328, 29–38. <https://doi.org/10.1016/j.epsl.2012.01.019>
- Leon-Rodriguez, L., & Dickens, G. R. (2010), Constraints on ocean acidification associated with rapid and massive carbon injections: The early Paleogene record at ocean drilling program site 1215, equatorial Pacific Ocean. *Palaeogeography, Palaeoclimatology, Palaeoecology*, 298(3–4), 409–420. <https://doi.org/10.1016/j.palaeo.2010.10.029>

- Littler, K., Röhl, U., Westerhold, T., & Zachos, J. C. (2014), A high-resolution benthic stable-isotope record for the South Atlantic: Implications for orbital-scale changes in Late Paleocene-Early Eocene climate and carbon cycling. *Earth and Planetary Science Letters*, 401, 18–30. <https://doi.org/10.1016/j.epsl.2014.05.054>
- Lourens, L. J., Sluijs, A., Kroon, D., Zachos, J. C., Thomas, E., Röhl, U., Bowles, J., & Raffi, I. (2005), Astronomical pacing of late Palaeocene to early Eocene global warming events. *Nature*, 435(7045), 1083–1087. <https://doi.org/10.1038/nature03814>
- Lu, Y., Makishima, A., & Nakamura, E. (2007), Coprecipitation of Ti, Mo, Sn and Sb with fluorides and application to determination of B, Ti, Zr, Nb, Mo, Sn, Sb, Hf and Ta by ICP-MS. *Chemical Geology*, 236(1–2), 13–26. <https://doi.org/10.1016/j.chemgeo.2006.08.007>
- Luciani, V., R Dickens, G., Backman, J., Fornaciari, E., Giusberti, L., Agnini, C., & D’Onofrio, R. (2016), Major perturbations in the global carbon cycle and photosymbiont-bearing planktic foraminifera during the early Eocene. *Climate of the Past*, 12(4), 981–1007. <https://doi.org/10.5194/cp-12-981-2016>
- Ma, Z., Gray, E., Thomas, E., Murphy, B., Zachos, J., & Paytan, A. (2014), Carbon sequestration during the Palaeocene-Eocene Thermal Maximum by an efficient biological pump. *Nature Geoscience*, 7(5), 382–388. <https://doi.org/10.1038/ngeo2139>
- Makishima, A., & Nakamura, E. (2006), Determination of Major/ Minor and Trace Elements in Silicate Samples by ICP-QMS and ICP-SFMS Applying Isotope Dilution-Internal Standardisation (ID-IS) and Multi-Stage Internal Standardisation. *Geostandards and Geoanalytical Research*, 30(3), 245–271. <https://doi.org/10.1111/j.1751-908X.2006.tb01066.x>
- Marchini, J. L., Heaton, C., & Ripley, B. D. (2013), Package ‘fastICA’ Reference manual. Retrieved from <http://cran.r-project.org/web/packages/fastICA/index.html>
- Martin, H. A. (2006), Cenozoic climatic change and the development of the arid vegetation in Australia. *Journal of Arid Environments*, 66(3), 533–563. <https://doi.org/10.1016/j.jaridenv.2006.01.009>
- Martini, E. (1971), Standard Tertiary and Quaternary calcareous nannoplankton zonation. In Farinacci, A., ed., *Proceedings of the Second Planktonic Conference Roma 1970*, Tecnoscienza, Roma, 739–785.
- McInerney, F. A., & Wing, S. L. (2011), The paleocene-eocene thermal maximum: A perturbation of carbon cycle, climate, and biosphere with implications for the future. *Annual Review of Earth and Planetary Sciences*, 39, 489–516. <https://doi.org/10.1146/annurev-earth-040610-133431>
- Miyazaki, T., Yasukawa, K., Tanaka, E., Vaglarov, B. S., & Yoshida, K. (2023), Ba stable isotope excursions induced by multiple hyperthermal events: A potential new index for transient global warming. *Geochemical Journal* 57(4), e1–e8. <https://doi.org/10.2343/geochemj.gj23011>
- Nicolo, M. J., Dickens, G. R., Hollis, C. J., & Zachos, J. C. (2007), Multiple early Eocene hyperthermals: Their sedimentary expression on the New Zealand continental margin and in the deep sea. *Geology*, 35(8), 699–702. <https://doi.org/10.1130/G23648A.1>
- Niederbockstruck, B., Jones, H. L., Yasukawa, K., Raffi, I., Tanaka, E., Westerhold, T., Ikehara, M., & Röhl, U. (2024), Apparent Diachroneity of Calcareous Nannofossil Datums During the Early Eocene in the High-Latitude South Pacific Ocean. *Paleoceanography and Paleoclimatology*, 39(4). <https://doi.org/10.1029/2023pa004801>
- O’Connor, J. M., Steinberger, B., Regelous, M., Koppers, A. A. P., Wijbrans, J. R., Haase, K. M., Stoffers, P., Jokat, W., & Garbe-Schönberg, D. (2013), Constraints on past plate and mantle motion from new ages for the Hawaiian-Emperor Seamount Chain. *Geochemistry, Geophysics, Geosystems*, 14(10), 4564–4584. <https://doi.org/10.1002/ggge.20267>
- Pälike, C., Delaney, M. L., & Zachos, J. C. (2014), Deep-sea redox across the Paleocene-Eocene thermal maximum. *Geochemistry, Geophysics, Geosystems*, 15, 1038–1053. <https://doi.org/10.1002/2013GC005074>.Received
- Pälike, H., Lyle, M. W., Nishi, H., Raffi, I., Ridgwell, A., Gamage, K., Klaus, A., Acton, G. et al. (2012), A Cenozoic record of the equatorial Pacific carbonate compensation depth. *Nature*, 488(7413), 609–614. <https://doi.org/10.1038/nature11360>
- Papadomanolaki, N. M., Sluijs, A., & Slomp, C. P. (2022), Eutrophication and Deoxygenation Forcing of Marginal Marine Organic Carbon Burial During the PETM. *Paleoceanography and Paleoclimatology*, 37(3). <https://doi.org/10.1029/2021PA004232>
- Pingitore, N. E., Eastman, M. P., Sandidge, M., Oden, K., & Freiha, B. (1988), The coprecipitation of manganese(II) with calcite: an experimental study. *Marine Chemistry*, 25(2), 107–120. [https://doi.org/10.1016/0304-4203\(88\)90059-x](https://doi.org/10.1016/0304-4203(88)90059-x)
- Plank, T., & Langmuir, C. H. (1998), The chemical composition of subducting sediment and its consequences for the crust and mantle. *Chemical Geology*, 145(3–4), 325–394. [https://doi.org/10.1016/S0009-2541\(97\)00150-2](https://doi.org/10.1016/S0009-2541(97)00150-2)

- Pogge von Strandmann, P. A. E., Jones, M. T., Joshua West, A., Murphy, M. J., Stokke, E. W., Tarbuck, G., Wilson, D. J., Pearce, C. R., & Schmidt, D. N. (2021), Lithium isotope evidence for enhanced weathering and erosion during the Paleocene-Eocene Thermal Maximum. *Science Advances*, 7(42), eabh4224. <https://doi.org/10.1126/sciadv.abh4224>
- Raffi, I., & De Bernardi, B. (2008), Response of calcareous nannofossils to the Paleocene-Eocene Thermal Maximum: Observations on composition, preservation and calcification in sediments from ODP Site 1263 (Walvis Ridge - SW Atlantic). *Marine Micropaleontology*, 69(2), 119–138. <https://doi.org/10.1016/j.marmicro.2008.07.002>
- Ravizza, G. E., & Zachos, J. C. (2014), Records of Cenozoic Ocean Chemistry. In *Treatise on Geochemistry: Second Edition* (Vol. 8, pp. 543–568). Elsevier Inc. <https://doi.org/10.1016/B978-0-08-095975-7.00620-3>
- Ravizza, G., Norris, R. N., Blusztajn, J., & Aubry, M. P. (2001), An osmium isotope excursion associated with the late Paleocene thermal maximum: Evidence of intensified chemical weathering. *Paleoceanography*, 16(2), 155–163. <https://doi.org/10.1029/2000PA000541>
- Reichgelt, T., Greenwood, D. R., Steinig, S., Conran, J. G., Hutchinson, D. K., Lunt, D. J., Scriven, L. J., & Zhu, J. (2022), Plant Proxy Evidence for High Rainfall and Productivity in the Eocene of Australia. *Paleoceanography and Paleoclimatology*, 37(6), e2022PA004418. <https://doi.org/10.1029/2022PA004418>
- Rivero-Cuesta, L., Westerhold, T., Agnini, C., Dallanave, E., Wilkens, R. H., & Alegret, L. (2019), Paleoenvironmental Changes at ODP Site 702 (South Atlantic): Anatomy of the Middle Eocene Climatic Optimum. *Paleoceanography and Paleoclimatology*, 34(12), 2047–2066. <https://doi.org/10.1029/2019pa003806>
- Rudnick, R. L., & Gao, S. (2014), Composition of the Continental Crust. In *Treatise on Geochemistry: Second Edition* (Vol. 4, pp. 1–51). Elsevier Inc. <https://doi.org/10.1016/B978-0-08-095975-7.00301-6>
- Scotese, C. R. (2001), Atlas of Earth history. PALEOMAP Project.
- Shamrock, J. L., & Watkins, D. K. (2012), Eocene calcareous nannofossil biostratigraphy and community structure from Exmouth Plateau, Eastern Indian Ocean (ODP Site 762). *Stratigraphy*, 9(1), 1–54.
- Shamrock, J. L., Watkins, D. K., & Johnston, K. W. (2012), Eocene biogeochronology and magnetostratigraphic revision of ODP Hole 762C, Exmouth Plateau (northwest Australian Shelf). *Stratigraphy* 9(1): 55–75.
- Sibert, E., Norris, R., Cuevas, J., & Graves, L. (2016), Eighty-five million years of Pacific Ocean gyre ecosystem structure: Long-term stability marked by punctuated change. *Proceedings of the Royal Society B: Biological Sciences*, 283(1831). <https://doi.org/10.1098/rspb.2016.0189>
- Siebert, C., Nägler, T. F., von Blanckenburg, F., & Kramers, J. D. (2003), Molybdenum isotope records as a potential new proxy for paleoceanography. *Earth and Planetary Science Letters*, 211(1–2), 159–171. [https://doi.org/10.1016/S0012-821X\(03\)00189-4](https://doi.org/10.1016/S0012-821X(03)00189-4)
- Siesser, W. G., & Bralower, T. J. (1992), Cenozoic calcareous nannofossil biostratigraphy on the Exmouth Plateau, eastern Indian Ocean. *Proc. Scientific Results, ODP, Leg 122, Exmouth Plateau*, 122, 601–731. <https://doi.org/10.2973/odp.proc.sr.122.162.1992>
- Slotnick, B. S., Lauretano, V., Backman, J., Dickens, G. R., Sluijs, A., & Lourens, L. (2015), Early Paleogene variations in the calcite compensation depth: New constraints using old borehole sediments from across Ninetyeast Ridge, central Indian Ocean. *Climate of the Past*, 11(3), 473–493. <https://doi.org/10.5194/cp-11-473-2015>
- Sluijs, A., Schouten, S., Donders, T. H., Schoon, P. L., Röhl, U., Reichert, G. J., Sangiorgi, F., Kim, J. H., Sinninghe Damsté, J. S., & Brinkhuis, H. (2009), Warm and wet conditions in the Arctic region during Eocene Thermal Maximum 2. *Nature Geoscience*, 2(11), 777–780. <https://doi.org/10.1038/ngeo668>
- Sluijs, A., Van Roij, L., Harrington, G. J., Schouten, S., Sessa, J. A., Levay, L. J., Reichert, G. J., & Slomp, C. P. (2014), Warming, euxinia and sea level rise during the paleocene-eocene thermal maximum on the gulf coastal plain: Implications for ocean oxygenation and nutrient cycling. *Climate of the Past*, 10(4), 1421–1439. <https://doi.org/10.5194/cp-10-1421-2014>
- Svensen, H., Planke, S., Maithe-Sørensen, A., Jamtveit, B., Myklebust, R., Eidem, T. R., & Rey, S. S. (2004), Release of methane from a volcanic basin as a mechanism for initial Eocene global warming. *Nature*, 429(6991), 542–545. <https://doi.org/10.1038/nature02566>
- Swanner, E. D., Webb, S. M., & Kappler, A. (2019), Fate of cobalt and nickel in mackinawite during diagenetic pyrite formation. *American Mineralogist*, 104(7), 917–928. <https://doi.org/10.2138/am-2019-6834>
- Takaya, Y., Yasukawa, K., Kawasaki, T., Fujinaga, K., Ohta, J., Usui, Y., Nakamura, K., Kimura, J. I., Chang, Q., Hamada, M., Doddiba, G., Nozaki, T., Iijima, K., Morisawa, T., Kuwahara, T., Ishida, Y., Ichimura, T., Kitazume, M., Fujita, T., & Kato, Y. (2018), The tremendous potential of deep-sea mud as a source of rare-earth elements. *Scientific Reports*, 8(1), 5763. <https://doi.org/10.1038/s41598-018-23948-5>

- Tanaka, E., Yasukawa, K., Ohta, J., & Kato, Y. (2022), Enhanced continental chemical weathering during the multiple early Eocene hyperthermals: New constraints from the southern Indian Ocean. *Geochimica et Cosmochimica Acta*, 331, 192–211. <https://doi.org/10.1016/j.gca.2022.05.022>
- Thomas, D. J., Bralower, T. J., & Jones, C. E. (2003), Neodymium isotopic reconstruction of late Paleocene-early Eocene thermohaline circulation. *Earth and Planetary Science Letters*, 209(3–4), 309–322. [https://doi.org/10.1016/S0012-821X\(03\)00096-7](https://doi.org/10.1016/S0012-821X(03)00096-7)
- Thomas, E. (1998), Biogeography of the Late Paleocene benthic foraminiferal extinction. In *Late Paleocene-early Eocene biotic and climatic events in the marine and terrestrial records* (pp. 214–243). Columbia University Press.
- Thomas, E., Shackleton, N. J., & Hall, M. A. (1992), Data Report: Carbon Isotope Stratigraphy of Paleogene Bulk Sediments, Hole 762C (Exmouth Plateau, Eastern Indian Ocean). In *Proceedings of the Ocean Drilling Program, Scientific Results* (Vol. 122, pp. 410–412). College Station, TX: Ocean Drilling Program. <https://doi.org/10.2973/odp.proc.sr.122.195.1992>
- Thomson, J., Higgs, N. C., Croudace, I. W., Colley, S., & Hydes, D. J. (1993), Redox zonation of elements at an oxic/post-oxic boundary in deep-sea sediments. *Geochimica et Cosmochimica Acta*, 57(3), 579–595. [https://doi.org/10.1016/0016-7037\(93\)90369-8](https://doi.org/10.1016/0016-7037(93)90369-8)
- Thomson, J., Higgs, N. C., Jarvis, I., Hydes, D. J., Colley, S., & Wilson, T. R. S. (1986), The behaviour of manganese in Atlantic carbonate sediments. *Geochimica et Cosmochimica Acta*, 50(8), 1807–1818. [https://doi.org/10.1016/0016-7037\(86\)90140-7](https://doi.org/10.1016/0016-7037(86)90140-7)
- Toyoda, K. & Tokonami, M. (1990), Diffusion of rare-earth elements in fish teeth from deep-sea sediments. *Nature* 345, 607–609.
- Tremolada, F., & Bralower, T. J. (2004), Nannofossil assemblage fluctuations during the Paleocene-Eocene Thermal Maximum at Sites 213 (Indian Ocean) and 401 (North Atlantic Ocean): Palaeoceanographic implications. *Marine Micropaleontology*, 52(1–4), 107–116. <https://doi.org/10.1016/j.marmicro.2004.04.002>
- Tripathi, A., & Elderfield, H. (2005), Deep-Sea Temperature and Circulation Changes at the Paleocene-Eocene Thermal Maximum. *Science*, 308(5730), 1894–1898. <https://doi.org/10.1126/science.1109202>
- Westerhold, T., Marwan, N., Drury, A. J., Liebrand, D., Agnini, C., Anagnostou, E., Barnett, J. S. K. et al. (2020), An astronomically dated record of Earth’s climate and its predictability over the last 66 million years. *Science*, 369(6509), 1383–1388. <https://doi.org/10.1126/SCIENCE.ABA6853>
- Westerhold, T., Röhl, U., Donner, B., & Zachos, J. C. (2018), Global Extent of Early Eocene Hyperthermal Events: A New Pacific Benthic Foraminiferal Isotope Record From Shatsky Rise (ODP Site 1209). *Paleoceanography and Paleoclimatology*, 33(6), 626–642. <https://doi.org/10.1029/2017PA003306>
- Westerhold, T., Röhl, U., Frederichs, T., Agnini, C., Raffi, I., Zachos, J. C., & Wilkens, R. H. (2017), Astronomical calibration of the Ypresian timescale: Implications for seafloor spreading rates and the chaotic behavior of the solar system? *Climate of the Past*, 13(9), 1129–1152. <https://doi.org/10.5194/cp-13-1129-2017>
- Whittaker, J. M., Müller, R. D., Leitchnikov, G., Stagg, H., Sdrolias, M., Gaina, C., & Goncharov, A. (2007), Major Australian-Antarctic plate reorganization at Hawaiian-Emperor bend time. *Science*, 318(5847), 83–86. <https://doi.org/10.1126/science.1143769>
- Willard, D. A., Donders, T. H., Reichgelt, T., Greenwood, D. R., Sangiorgi, F., Peterse, F., Nierop, K. G. J., Frieling, J., Schouten, S., & Sluijs, A. (2019), Arctic vegetation, temperature, and hydrology during Early Eocene transient global warming events. *Global and Planetary Change*, 178(4), 139–152. <https://doi.org/10.1016/j.gloplacha.2019.04.012>
- Winguth, A. M. E., Thomas, E., & Winguth, C. (2012), Global decline in ocean ventilation, oxygenation, and productivity during the Paleocene-Eocene Thermal Maximum: Implications for the benthic extinction. *Geology*, 40(3), 263–266. <https://doi.org/10.1130/G32529.1>
- Xu, K., De Vleeschouwer, D., Vahlenkamp, M., Yang, R., & Chen, H. (2021), Reconstructing Eocene Eastern Indian Ocean dynamics using ocean-drilling stratigraphic records. *Paleoceanography and Paleoclimatology*, 36, e2020PA004116. <https://doi.org/10.1029/2020pa004116>
- Yasukawa, K., Kino, S., Azami, K., Tanaka, E., Mimura, K., Ohta, J., Fujinaga, K., Nakamura, K., & Kato, Y. (2020), Geochemical features of Fe-Mn micronodules in deep-sea sediments of the western North Pacific Ocean: Potential for co-product metal extraction from REY-rich mud. *Ore Geology Reviews*, 127, 103805. <https://doi.org/10.1016/j.oregeorev.2020.103805>
- Yasukawa, K., Nakamura, K., Fujinaga, K., Ikehara, M., & Kato, Y. (2017), Earth system feedback statistically extracted from the Indian Ocean deep-sea sediments recording Eocene hyperthermals. *Scientific Reports*, 7(1), 11304. <https://doi.org/10.1038/s41598-017-11470-z>

- 1189 Yasukawa, K., Nakamura, K., Fujinaga, K., Iwamori, H., & Kato, Y. (2016), Tracking the spatiotemporal variations
1190 of statistically independent components involving enrichment of rare-earth elements in deep-sea sediments. In
1191 *Scientific Reports*, 6(1), 29603. <https://doi.org/10.1038/srep29603>
- 1192 Yasukawa, K., Ohta, J., Hamada, M., Chang, Q., Nakamura, H., Ashida, K., Takaya, Y., Nakamura, K., Iwamori,
1193 H., & Kato, Y. (2022), Essential processes involving REE-enrichment in biogenic apatite in deep-sea sediment
1194 decoded via multivariate statistical analyses. *Chemical Geology*, 614, 121184.
1195 <https://doi.org/10.1016/j.chemgeo.2022.121184>
- 1196 Yasukawa, K., Ohta, J., Miyazaki, T., Vaglarov, B. S., Chang, Q., Ueki, K., Toyama, C., Kimura, J. I., Tanaka, E.,
1197 Nakamura, K., Fujinaga, K., Iijima, K., Iwamori, H., & Kato, Y. (2019), Statistic and Isotopic
1198 Characterization of Deep-Sea Sediments in the Western North Pacific Ocean: Implications for Genesis of the
1199 Sediment Extremely Enriched in Rare Earth Elements. *Geochemistry, Geophysics, Geosystems*, 20(7), 3402–
1200 3430. <https://doi.org/10.1029/2019GC008214>
- 1201 Yasukawa, K., Tanaka, E., Miyazaki, T., Vaglarov, B. S., Chang, Q., Nakamura, K., Ohta, J., Fujinaga, K., Iwamori,
1202 H., & Kato, Y. (2023), R script for k-means cluster analysis with whitening and projection pursuit for a
1203 chemical composition dataset of pelagic clay around Minamitorishima Island in the western North Pacific
1204 Ocean. [Software]. *Zenodo*. <https://doi.org/10.5281/zenodo.8098551>
- 1205 Zachos, J. C., McCarren, H., Murphy, B., Röhl, U., & Westerhold, T. (2010), Tempo and scale of late Paleocene and
1206 early Eocene carbon isotope cycles: Implications for the origin of hyperthermals. *Earth and Planetary Science
1207 Letters*, 299(1–2), 242–249. <https://doi.org/10.1016/j.epsl.2010.09.004>
- 1208 Zachos, J. C., Röhl, U., Schellenberg, S. A., Sluijs, A., Hodell, D. A., Kelly, D. C., Thomas, E., Nicolo, M., Raffi, I.,
1209 Lourens, L. J., McCarren, H., & Kroon, D. (2005), Paleoclimate: Rapid acidification of the ocean during the
1210 paleocene-eocene thermal maximum. *Science*, 308(5728), 1611–1615.
1211 <https://doi.org/10.1126/science.1109004>
- 1212 Zachos, J. C., Wara, M. W., Bohaty, S., Delaney, M. L., Petrizzo, M. R., Brill, A., Bralower, T. J., & Premoli-Silva,
1213 I. (2003), A Transient Rise in Tropical Sea Surface Temperature during the Paleocene-Eocene Thermal
1214 Maximum. *Science*, 302(5650), 1551–1554. <https://doi.org/10.1126/science.1090110>
- 1215 Zachos, J., Pagani, H., Sloan, L., Thomas, E., & Billups, K. (2001), Trends, rhythms, and aberrations in global
1216 climate 65 Ma to present. *Science*, 292(5517), 686–693. <https://doi.org/10.1126/science.1059412>
- 1217 Zhou, X., Thomas, E., Rickaby, R. E. M., Winguth, A. M. E., & Lu, Z. (2014), I/Ca evidence for upper ocean
1218 deoxygenation during the PETM. *Paleoceanography*, 29(10), 964–975. <https://doi.org/10.1002/2014pa002702>
- 1219 Zhou, X., Thomas, E., Winguth, A. M. E., Ridgwell, A., Scher, H., Hoogakker, B. A. A., Rickaby, R. E. M., & Lu,
1220 Z. (2016), Expanded oxygen minimum zones during the late Paleocene-early Eocene: Hints from multiproxy
1221 comparison and ocean modeling. *Paleoceanography*, 31(12), 1532–1546.
1222 <https://doi.org/10.1002/2016PA003020>